J. Mech. Phys. Solids 194 (2025) 105930

Contents lists available at ScienceDirect

Journal of the Mechanics and Physics of Solids

journal homepage: www.elsevier.com/locate/jmps

Modeling yield stress scaling and cyclic response using a size-dependent theory with two plasticity rate fields

Andrea Panteghini [a], Lorenzo Bardella [a,*], M.B. Rubin [b]

[a] Department of Civil, Environmental, Architectural Engineering and Mathematics (DICATAM), University of Brescia, Italy
[b] Faculty of Mechanical Engineering, Technion-Israel Institute of Technology, 32000 Haifa, Israel

ARTICLE INFO

Keywords:
Small-scale metal plasticity
Strengthening and mechanisms
Size effect
Yield stress scaling
Finite element method
Finite strain
Non-proportional loading

ABSTRACT

This work considers a recently developed finite-deformation elastoplasticity theory that assumes distinct tensorial fields describing *macro*-plasticity and *micro*-plasticity, where the latter is determined by a higher-order balance equation with associated boundary conditions. Specifically, *micro*-plasticity evolves according to a contribution to the Helmholtz free-energy density that depends on a Nye–Kröner-like dislocation density tensor and is referred to as the *defect energy*. The theory is meant to set the onset of micro-plasticity at a stress level lower than that activating macro-plasticity, such as micro-plasticity aims at explaining and characterizing the increase in yield stress with diminishing size. Additionally, the formulation relies on smooth elastic–plastic transitions for both plasticity fields, even if focusing on rate-independent response. This investigation demonstrates the capability of the proposed theory to predict size-effects of interest in small-scale metal plasticity by focusing on multiple loading cycles and, prominently, on the scaling of the *apparent* yield stress with sample size, the latter being a crucial open issue in the recent literature on modeling size-dependent plasticity. To this end, this work considers the specialization of the theory to small deformations and proposes a finite element implementation for the constrained simple shear problem. Importantly, it is shown that the simplest treatment of plastic strain gradients, which consists of adopting a quadratic defect energy, can be conveniently used to predict reliable size-effects, although in the literature on strain gradient plasticity quadratic defect energies have always been associated with a relatively poor description of size-effects. In fact, in the present theory the limits of the quadratic defect energy are overcome by leveraging on the complex interplay between micro- and macro-plasticity fields. The capability of the proposed theory is quantitatively demonstrated by predicting results from the literature that are obtained from discrete dislocation dynamics simulations on planar polycrystals of grains with variable size subjected to macroscopic pure shear.

1. Introduction

This work investigates the size-dependent elastoplasticity theory developed in (Rubin and Bardella, 2023), henceforth denoted as "m$\mathcal{M}$ theory", by referring to its fundamental feature of including two plasticity fields, namely micro-plasticity and macro-plasticity. While, in this theory, macro-plasticity is determined by a standard plastic rate tensor, micro-plasticity is governed by a higher-order balance that relies on the strain gradient plasticity (SGP) developed by Gurtin (2004). Consequently, the theory involves the Nye–Kröner tensor (Nye, 1953; Kröner, 1962) to phenomenologically account for the effect of densities of geometrically necessary

* Corresponding author.
E-mail addresses: andrea.panteghini@unibs.it (A. Panteghini), lorenzo.bardella@ing.unibs.it (L. Bardella), mbrubin@tx.technion.ac.il (M.B. Rubin).

https://doi.org/10.1016/j.jmps.2024.105930
Received 9 August 2024; Received in revised form 27 October 2024; Accepted 31 October 2024

Available online 8 November 2024

dislocations (GNDs, Ashby, 1970), which leads to the "smaller is stronger" size-effect in a size range spanning from a few tens of nanometers to a few tens of micrometers (Fleck and Hutchinson, 1997; Greer and De Hosson, 2011; Mu et al., 2016).

The m$\mathcal{M}$ theory, which is summarized in Section 2, is built on the idea that micro-plastic flow diminishes with decrease in specimen size and its interplay with macro-plasticity leads to the observed strengthening. This is achieved by simply imposing that the initial micro-yield stress is appropriately lower than the macro-yield stress. The proposed use of the micro-plastic field is inspired by the experimental results of Maaß and Derlet (2018) and references therein, which explain the strengthening through the observation of irreversible, tiny deformations, which are referred to as "micro-plastic" deformations, occurring before the onset of *apparent* (or "macroscopic") yield. Importantly, in the m$\mathcal{M}$ theory the onsets of micro- and macro-plasticity are both accompanied by a rate-independent smooth transition between the elastic and plastic regimes. With these evolution equations, the m$\mathcal{M}$ theory introduces a physical mechanism that causes the strengthening experimentally observed (Fleck et al., 1994; Greer and De Hosson, 2011; Liu et al., 2013; Mu et al., 2016). In the *non-incremental* theories, so called by Fleck et al. (2014) to denote a class of SGP theories that have been developed since the fundamental contributions of Gudmundson (2004) and Gurtin (2004), that physical mechanism is lacking, being substituted by subtle mathematics (Chiricotto et al., 2016) allowing the prediction of strengthening at the price of anomalous behaviors under certain non-proportional loading histories (Fleck et al., 2014).

Additionally, the m$\mathcal{M}$ theory has been developed for large deformations by using an Eulerian formulation of the constitutive equations. Such formulation is independent of arbitrary specifications of a total strain measure, of a plastic strain measure, and of reference and intermediate configurations (Rubin, 1996, 2012, 2021). In particular, avoiding the Bilby–Kröner–Lee multiplicative form of the deformation gradient (Bilby et al., 1957; Kröner, 1959; Lee, 1969) is particularly convenient since a Lagrangian formulation of the proposed model would introduce additional arbitrariness due to the presence of three distinct deformation fields (elastic, micro-plastic, and macro-plastic). However, in the present investigation results are obtained for the specialization of the m$\mathcal{M}$ theory to small-deformations, thus using a theory that is central for and common to any of its possible extensions to the finite-deformation regime.

In (Rubin and Bardella, 2023), the m$\mathcal{M}$ theory has been tested through semi-analytical solutions for the constrained simple shear problem, where plastic strain gradients are triggered by *microhard* boundary conditions, hampering plastic flow at the boundary. Because of its simplicity and its capability to highlight several important features of SGP theories, this boundary value problem has been adopted to test new theories for more than twenty years (see, e.g., Bittencourt et al., 2003; Niordson and Hutchinson, 2003). Also, since the work of Mu et al. (2014), the constrained simple shear has become a reference benchmark problem to discuss the outcome of experimental tests where plastic flow localizes in thin films. Obtaining the semi-analytical solutions in (Rubin and Bardella, 2023) requires limiting the model to small strains and rotations, perfect micro-plasticity, perfect macro-plasticity, and monotonic loading. This investigation removes the assumption of perfect micro- and macro-plasticity by including hardening, and focuses also on multiple loading cycles. Under these circumstances, solutions are obtained using a finite element (FE) implementation of the m$\mathcal{M}$ theory for constrained simple shear within small strains and rotations. This is illustrated in Section 3.2 after the weak form of the balance equations and the backward Euler time-integration scheme are provided in Section 3.1 for general stress states. Note that the kinematics-based FE formulation of the m$\mathcal{M}$ theory requires, as nodal degrees of freedom (DOFs), the displacement components plus the $H(\mathrm{curl})$ micro-plastic variables (Panteghini and Bardella, 2018) due to the use of Nye–Kröner tensor, as in Gurtin (2004) SGP theory. In fact, macro-plasticity does not require additional DOFs, being conventionally dealt with in each Gauss point when integrating the constitutive equations.

As a further novelty, to model the response under non-proportional loading, in this work the smooth transition between the elastic and micro-plastic regimes is modified with respect to the proposal in (Rubin and Bardella, 2023). In this regard, however, the main general features of the m$\mathcal{M}$ theory are preserved: that smooth transition is still governed by the non-dimensional function $\Gamma_G \geq 0$ entering the micro-plasticity rate $\Gamma_G\mathbf{G}$, where $\mathbf{G}$ is a traceless second-order tensor and, for small deformations, Γ_G is a function of the equivalent von Mises stress σ_e. Additionally, Γ_G enters also the higher-order micro-plasticity balance equation, which turns out to hold, along with the constitutive equations for the stresses entering it, always, independent of the loading history; this is not the case in "conventional" rate-independent higher-order SGP (Nielsen and Niordson, 2014, 2019; Willis, 2019). In (Rubin and Bardella, 2023) Γ_G is a history-independent function that may increase or decrease with σ_e and may assume any non-negative value, while here, for the reasons documented in detail in Appendix C, Γ_G is proposed to be a function of σ_e that monotonically increases to its saturated value, as specified in Section 2.5. Also, the micro-plasticity rate $\Gamma_G\mathbf{G}$ is a non-symmetric tensor, thus allowing the theory to account for the contribution, partly energetic and partly dissipative, of the micro-plastic spin rate, which plays an important role in modeling small-scale plasticity (Bardella, 2009, 2010; Bardella and Panteghini, 2015; Poh and Peerlings, 2016; Ebobisse et al., 2019; Rubin and Bardella, 2024).

As shown by the results presented in Section 4, the proposed use of two plasticity fields holds promise to allow modeling size-effects observed in experiments and in discrete dislocation dynamics (DDD) simulations. First, in Section 4.1, the flexibility of the m$\mathcal{M}$ theory to predict reliable responses under multiple loading cycles is demonstrated by studying the influence of varying some key material parameters. More importantly, modeling the scaling of the *apparent* yield stress with the sample size (Biner and Morris, 2002; Balint et al., 2005; El-Awady et al., 2013; Li et al., 2022; Zhang et al., 2023; Cruzado et al., 2024; Amouzou-Adoun et al., 2024) has been an open issue in higher-order SGP since the study of Dunstan and Bushby (2014) and the experimental observations of Mu et al. (2014). In this regard, Section 4.2 shows that the m$\mathcal{M}$ theory can control the correct scaling by adjusting the initial micro- and macro-yield stresses while adopting the simplest possible treatment of plastic strain gradients, that is a quadratic *defect energy*. By following Gurtin's terminology, the defect energy is the function of the higher-order primal variable (here, the Nye–Kröner tensor) that extends the conventional Helmholtz free-energy density. This approach of the m$\mathcal{M}$ theory, although being phenomenological, is convenient in comparison to other efforts to develop thermodynamically-consistent SGP models that can (or exhibit potential

to) predict the correct scaling of the apparent yield stress and are also free from typical drawbacks of SGP (discussed in the literature since Fleck et al., 2014). These efforts require either to resort to finer scale theories such as mesoscale field dislocation mechanics (Arora et al., 2022) or sophisticated and expensive techniques involving plastic strain gradients to describe the material behavior in the bulk (Panteghini et al., 2019; Dahlberg and Ortiz, 2019; Panteghini and Bardella, 2020; Bardella, 2021; Khandagale et al., 2024) and at interfaces (Kuroda et al., 2021; Kuroda and Needleman, 2023).

Additionally, Section 4.3 illustrates the capability of the m$\mathcal{M}$ theory to predict the stress–strain curves obtained by Balint et al. (2005) through DDD simulations of the response of planar polycrystals with variable grains' size and subjected to macroscopic pure shear. This is remarkable as these stress–strain curves exhibit both strengthening and increase in strain hardening with diminishing size. Concluding remarks are offered in Section 5.

2. Summary of the m$\mathcal{M}$ theory

This section summarizes the finite-deformation m$\mathcal{M}$ theory by restricting attention to isothermal conditions. Its specialization to small strains and rotations is provided in Section 2.6.

2.1. Kinematics for elastically isotropic response dependent on the dislocation density tensor

By denoting with $\dot{(\,)}$ material time differentiation,

$$\mathbf{v} = \dot{\mathbf{x}}$$

is the velocity of material point located at the current position $\mathbf{x}$ at time t.

One of the basic postulates of the theory extends the finite-deformation elastoplasticity in (Rubin and Attia, 1996) by adding a micro-plastic rate tensor in the following evolution equation for the elastic distortional deformation, which is determined by the symmetric second-order tensor $\bar{\mathbf{B}}_e$:

$$\dot{\bar{\mathbf{B}}}_e = \mathbf{L}'\bar{\mathbf{B}}_e + \bar{\mathbf{B}}_e\mathbf{L}'^T - \Gamma\mathbf{A}_p - \Gamma_G\mathbf{A}_G\,, \quad \mathbf{A}_p = \bar{\mathbf{B}}_e - \frac{3}{\mathrm{tr}(\bar{\mathbf{B}}_e^{-1})}\mathbf{I}\,, \quad \mathbf{A}_G = 2\big[{}_S\mathbf{G} - \frac{{}_S\mathbf{G}\cdot\bar{\mathbf{B}}_e^{-1}}{\mathrm{tr}(\bar{\mathbf{B}}_e^{-1})}\mathbf{I}\big]\,, \tag{1}$$

where $\bar{(\,)}$ denotes a unimodular tensor (i.e. $\dot{\bar{\mathbf{B}}}_e\cdot\bar{\mathbf{B}}_e^{-1} = 0$), $\mathbf{L} = \partial\mathbf{v}/\partial\mathbf{x}$ is the velocity gradient, the superscript $(\,)'$ denotes the deviatoric part of second-order tensors (such as $\mathbf{L}' = \mathbf{L} - \mathrm{tr}(\mathbf{L})\mathbf{I}/3$, with $\mathbf{I}$ denoting the second-order identity tensor), $\Gamma \geq 0$ is a function that provides the rate of macro-plasticity, whose direction is given by the non-dimensional second-order tensor $\mathbf{A}_p$, $\Gamma_G \geq 0$ is a non-dimensional function that modulates the magnitude of micro-plasticity, and $\mathbf{G}$ is the traceless micro-plasticity rate, which is an *independent* second-order tensor whose symmetric part is denoted as ${}_S\mathbf{G}$. Care should be taken to keep in mind that Γ and Γ_G have different units. Here and henceforth, $\mathbf{A}\cdot\mathbf{B} = \mathrm{tr}(\mathbf{A}\mathbf{B}^T)$ indicates the inner product of two second-order tensors $\mathbf{A}$ and $\mathbf{B}$.

In Eq. (1), $\mathbf{A}_p$ and $\mathbf{A}_G$ satisfy the restrictions $\mathbf{A}_p\cdot\bar{\mathbf{B}}_e^{-1} = 0$ and $\mathbf{A}_G\cdot\bar{\mathbf{B}}_e^{-1} = 0$, which ensure that $\bar{\mathbf{B}}_e$ remains unimodular. In the absence of plasticity, i.e. $\Gamma\mathbf{A}_p = \Gamma_G\mathbf{A}_G = \mathbf{0}$, Eq. (1) is the evolution equation for the distortional part of the left Cauchy–Green total deformation, that is a specialization to general isotropic hyperelasticity. Also, the functional form of the macro-plasticity rate is such that $\mathbf{A}_p = \mathbf{0}$ for $\bar{\mathbf{B}}_e = \mathbf{I}$, implying that macro-plasticity tends to diminish the deviatoric part of the Cauchy stress.

For later reference, it is convenient to introduce the first invariant β_1 of $\bar{\mathbf{B}}_e$,

$$\beta_1 = \mathrm{tr}(\bar{\mathbf{B}}_e)\,. \tag{2}$$

The elastic dilatation J_e satisfies the evolution equation

$$\frac{\dot{J}_e}{J_e} = \mathrm{tr}(\mathbf{D})\,, \tag{3}$$

where $\mathbf{D} = (\mathbf{L} + \mathbf{L}^T)/2$ is the rate of deformation.

The evolution equation for the second-order Nye–Kröner-like dislocation density tensor $\boldsymbol{\alpha}$, which models densities of geometrically necessary dislocations (GNDs) in metal plasticity (Ashby, 1970; Fleck and Hutchinson, 1997; Arsenlis and Parks, 1999; Gurtin, 2004), can be expressed through its Jaumann derivative as[1]

$$\mathring{\boldsymbol{\alpha}} = \mathbf{W}\boldsymbol{\alpha} + \boldsymbol{\alpha}\mathbf{W}^T + \mathrm{curl}\,\mathbf{G} - a|\mathbf{D}'_p|\boldsymbol{\alpha}\,, \tag{4}$$

where $\mathbf{W} = (\mathbf{L} - \mathbf{L}^T)/2$ is the rate of spin, the last term models annihilation of defects, which is controlled by the constant $a \geq 0$ and is driven by the magnitude, $|\mathbf{D}'_p| = \sqrt{\mathbf{D}'_p\cdot\mathbf{D}'_p}$, of the macro-plasticity rate of deformation $\mathbf{D}'_p = \Gamma\bar{\mathbf{B}}'_e/2$. Note that the term $|\mathbf{D}'_p|\boldsymbol{\alpha}$ and those involving the spin rate contribute to Eq. (4) only within finite deformations. Hence, although $\boldsymbol{\alpha}$ mostly depends on micro-plasticity, the term $|\mathbf{D}'_p|\boldsymbol{\alpha}$ couples, through the parameter $a > 0$, macro- and micro-plasticity for suitably large plastic flow. This contributes to model the interaction between the two plasticity fields, allowing for smoothing out the effect of micro-plasticity alone through the possibility of dislocation densities from macro-plasticity to combine and annihilate with those from micro-plasticity.

[1] By referring to a fixed orthonormal Cartesian triad $\mathbf{e}_i$, $\mathrm{curl}\,\mathbf{G}$ is defined such as $(\mathrm{curl}\,\mathbf{G})\cdot(\mathbf{e}_i\otimes\mathbf{e}_j) \equiv \epsilon_{jkl}\partial G_{il}/\partial x_k$, where $\mathbf{a}\otimes\mathbf{b}$ indicates the tensor product between two vectors $\mathbf{a}$ and $\mathbf{b}$, $\epsilon_{ijk} = (i-j)(j-k)(k-i)/2$ is the Ricci–Curbastro third-order tensor, $G_{ij} = \mathbf{G}\cdot(\mathbf{e}_i\otimes\mathbf{e}_j)$, $x_i = \mathbf{x}\cdot\mathbf{e}_i$, and summation convention over repeated indices is adopted.

The study of this coupling is left for future investigations, as here focus is on micro- and macro-hardening within small strains and rotations.

The higher-order constitutive equations in the m$\mathcal{M}$ theory use the three invariants of $\boldsymbol{\alpha}$

$$\alpha_1 = [\mathrm{tr}(\boldsymbol{\alpha})]^2\,, \quad \alpha_2 = {}_S\boldsymbol{\alpha}' \cdot {}_S\boldsymbol{\alpha}'\,, \quad \alpha_3 = {}_{SK}\boldsymbol{\alpha} \cdot {}_{SK}\boldsymbol{\alpha}\,, \tag{5}$$

where ${}_S\boldsymbol{\alpha}' = (\boldsymbol{\alpha}' + \boldsymbol{\alpha}'^T)/2$ and ${}_{SK}\boldsymbol{\alpha} = (\boldsymbol{\alpha} - \boldsymbol{\alpha}^T)/2$.

Next, the local forms of the balance laws are presented. For the global forms, the reader is referred to (Rubin and Bardella, 2023).

2.2. Local forms of the balance laws

The local forms of two conventional balance laws are

$$\dot{\rho} + \rho\,\mathrm{tr}(\mathbf{D}) = 0\,, \quad \rho\dot{\mathbf{v}} = \rho\mathbf{b} + \mathrm{div}\mathbf{T}\,,$$

where ρ is the current mass density, $\mathbf{b}$ is the specific (per unit mass) externally applied body force, and $\mathbf{T}$ denotes the Cauchy stress. Also, the conservation of mass is satisfied when $J_e = \rho_z/\rho$, with ρ_z denoting the material zero-stress density at reference temperature.

The local form of the balance of angular momentum establishes that the Cauchy stress tensor is symmetric, $\mathbf{T}^T = \mathbf{T}$, and the local form of the balance of micro-plasticity results

$$(\mathrm{curl}\,\boldsymbol{\zeta})' + \mathbf{S} - \mathbf{M} = \mathbf{0}\,. \tag{6}$$

In this equation, $\boldsymbol{\zeta}$ is a second-order tensor constitutively dependent on $\boldsymbol{\alpha}$, such that $\boldsymbol{\zeta}$ has the dimension of force per unit length. Also, $\mathbf{S}$ is a dissipative second-order stress tensor conjugate to $\mathbf{G}$ and $\mathbf{M}$ is an energetic second-order stress tensor conjugate to ${}_S\mathbf{G}$, such that $\mathbf{M}^T = \mathbf{M}$, $\mathrm{tr}(\mathbf{M}) = 0$, $\mathrm{tr}(\mathbf{S}) = 0$. Eq. (6) can be conveniently split into its symmetric and skew-symmetric parts:

$${}_S\mathbf{S} = \mathbf{M} - {}_S(\mathrm{curl}\,\boldsymbol{\zeta})'\,, \quad {}_{SK}\mathbf{S} = -{}_{SK}(\mathrm{curl}\,\boldsymbol{\zeta})\,. \tag{7}$$

The higher-order balance law (6) requires micro-plasticity boundary conditions. This investigation is concerned with homogeneous kinematic higher-order boundary conditions only, that are imposed of the boundary subset ∂P_k as[2]

$$\mathbf{G} \times \mathbf{n} = \mathbf{0} \quad \text{on} \quad \partial P_k\,. \tag{8}$$

Such boundary conditions are referred to as "microhard" and model an impenetrable boundary where dislocations pile up and form densities of GNDs (Fleck and Hutchinson, 1997; Gurtin, 2004).

2.3. General constitutive equations for the stresses

By focusing on isothermal conditions, the Helmholtz free energy ψ for elastically isotropic response is assumed to be a function of the elastic dilatation in Eq. (3) and of the invariants defined in Eqs. (2) and (5),

$$\psi = \psi(J_e, \beta_1, \alpha_1, \alpha_2, \alpha_3)\,,$$

with the restrictions

$$\frac{\partial\psi}{\partial\beta_1} > 0\,, \quad \frac{\partial\psi}{\partial\alpha_1} \geq 0\,, \quad \frac{\partial\psi}{\partial\alpha_2} \geq 0\,, \quad \frac{\partial\psi}{\partial\alpha_3} \geq 0\,, \tag{9}$$

such that the general constitutive equations for the recoverable stresses are given by

$$\begin{aligned} &p = -\rho_z \frac{\partial\psi}{\partial J_e}\,, \quad \mathbf{T}' = 2\rho_z J_e^{-1} \frac{\partial\psi}{\partial\beta_1}\bar{\mathbf{B}}_e'\,, \quad \mathbf{M} = -2\rho_z J_e^{-1} \frac{\partial\psi}{\partial\beta_1} \frac{3}{\mathrm{tr}(\bar{\mathbf{B}}_e^{-1})} \Gamma_G (\bar{\mathbf{B}}_e^{-1})'\,, \\ &\boldsymbol{\zeta} = 2\rho_z J_e^{-1} \Big[\frac{\partial\psi}{\partial\alpha_1}\,\mathrm{tr}(\boldsymbol{\alpha})\,\mathbf{I} + \frac{\partial\psi}{\partial\alpha_2}\,{}_S\boldsymbol{\alpha}' + \frac{\partial\psi}{\partial\alpha_3}\,{}_{SK}\boldsymbol{\alpha} \Big]\,, \end{aligned} \tag{10}$$

where $p = -\mathrm{tr}(\mathbf{T})/3$ is the pressure. It is convenient to define the invariant σ_M of $\mathbf{M}$ as

$$\sigma_M \equiv 2\rho_z J_e^{-1} \frac{\partial\psi}{\partial\beta_1} \frac{3}{\mathrm{tr}(\bar{\mathbf{B}}_e^{-1})} \sqrt{\frac{3}{2}}\,|(\bar{\mathbf{B}}_e^{-1})'|\,. \tag{11}$$

Note that the energetic stress $\mathbf{M}$ provides essential coupling between macro- and micro-plasticity in the micro-plasticity balance (6).

The dissipative stress $\mathbf{S}$ is prescribed by following Gurtin (2004) as

$$\begin{aligned} &{}_S\mathbf{S} = \frac{2}{3}\Gamma_G S \frac{{}_S\mathbf{G}}{G}\,, && {}_{SK}\mathbf{S} = \chi\Gamma_G S \frac{{}_{SK}\mathbf{G}}{G}\,, \\ &\Gamma_G S = \sqrt{\frac{3}{2}|{}_S\mathbf{S}|^2 + \frac{1}{\chi}|{}_{SK}\mathbf{S}|^2} \geq 0\,, && G = \sqrt{\frac{2}{3}|{}_S\mathbf{G}|^2 + \chi|{}_{SK}\mathbf{G}|^2} \geq 0\,, \end{aligned} \tag{12}$$

[2] With $\boldsymbol{\zeta}$ and $\mathbf{n}$ denoting a second-order tensor and a vector, respectively, the product $\boldsymbol{\zeta} \times \mathbf{n}$ is defined such as $(\boldsymbol{\zeta} \times \mathbf{n}) \cdot (\mathbf{e}_i \otimes \mathbf{e}_j) \equiv \epsilon_{jlk}\zeta_{il}n_k$.

where $\mathbf{S}$ is separated into its symmetric, ${}_S\mathbf{S}$, and skew-symmetric, ${}_{SK}\mathbf{S}$, parts and $\chi \geq 0$ is a parameter governing the dissipation associated with the micro-plasticity spin rate. A feature distinguishing this formulation from other SGP theories (Gudmundson, 2004; Gurtin, 2004) is that the function $\Gamma_G \geq 0$ entering the evolution equation for the distortional deformation (1) is introduced also in the constitutive equations for $\mathbf{S}$. This allows both for a smooth transition between the elastic and micro-plastic regimes and for the micro-plasticity balance (6) to be used and solved, together with rate-independent constitutive laws, all along any loading path. In this investigation, with respect to (Rubin and Bardella, 2023), a new proposal for the constitutive equation for Γ_G will be specified in Section 2.5 in order to model non-proportional loading histories.

The foregoing constitutive theory satisfies the second law of thermodynamics because of the restrictions in Eq. (9), because Eq. (12) leads to $\mathbf{S}\cdot\mathbf{G} = {}_S\mathbf{S}\cdot{}_S\mathbf{G} + {}_{SK}\mathbf{S}\cdot{}_{SK}\mathbf{G} = \Gamma_G S G \geq 0$, and because $\mathrm{tr}(\mathbf{A}_p) \geq 0$ holds (Rubin and Attia, 1996).

In (Rubin and Bardella, 2023), it is further shown that all the fields of interest in this theory satisfy the required invariance under superposed rigid body motions.

2.4. A convenient, specific form of the Helmholtz free energy

This work considers the isothermal Helmholtz free energy ψ

$$\rho_z\psi = k\big[J_e - 1 - \ln(J_e)\big] + \frac{1}{2}\mu(\beta_1 - 3) + \Psi_{\mathrm{d}}(\boldsymbol{\alpha}), \quad \Psi_{\mathrm{d}}(\boldsymbol{\alpha}) = \frac{1}{2}\mu\ell^2(k_1\alpha_1 + k_2\alpha_2 + k_3\alpha_3), \tag{13}$$

where $k > 0$ and $\mu > 0$ are the zero-stress bulk and shear moduli, respectively, and $\Psi_{\mathrm{d}}(\boldsymbol{\alpha})$ is the defect energy, which is characterized by material length $\ell \geq 0$ and, additionally, by the dimensionless constants $k_1 \geq 0, k_2 \geq 0, k_3 \geq 0$ controlling $\Psi_{\mathrm{d}}(\boldsymbol{\alpha})$ through the three independent parameters $\ell^2 k_1, \ell^2 k_2, \ell^2 k_3$.

In the light of the literature on SGP, it is important to note that the defect energy is specified to be quadratic in the higher-order primal variable. Size-effects in small-scale metal plasticity are often discussed by focusing on two features, with diminishing size: the increase in strain hardening and the increase in what is recognized as the yield point from a kink in the macroscopic stress–strain curve, the latter effect being usually referred to as strengthening. The strengthening is particularly important as it sets the scaling with size of the *apparent* yield stress. Although quadratic defect energies are the most convenient potentials from the computational point of view, they are known to suffer the drawback that they predict, in most cases, negligible strengthening, which is instead clearly observed in experiments (Fleck et al., 1994; Greer and De Hosson, 2011; Liu et al., 2013; Mu et al., 2014; Zhang et al., 2023).[3] This investigation shows that the m$\mathcal{M}$ theory overcomes this limit of quadratic defect energies thanks to the interplay between the onsets of micro- and macro-plasticity.

Specifically, this is achieved by setting the initial macro-yield stress to be larger than the stress level activating micro-plasticity. Given that micro-plasticity models the behavior of GND densities, a proper calibration of the material parameters allows the micro-plasticity developed before macro-plasticity to control the observed strengthening, consistently with experimental observations (Maaß and Derlet, 2018).

From (10) and (13), the energetic stresses are given by

$$p = k\Big(\frac{1}{J_e} - 1\Big), \quad \mathbf{T}' = J_e^{-1}\mu\bar{\mathbf{B}}_e', \quad \mathbf{M} = -J_e^{-1}\mu\frac{3}{\mathrm{tr}(\bar{\mathbf{B}}_e^{-1})}\Gamma_G(\bar{\mathbf{B}}_e^{-1})', \quad \boldsymbol{\zeta} = J_e^{-1}\mu\ell^2\big[k_1\,\mathrm{tr}(\boldsymbol{\alpha})\,\mathbf{I} + k_2\,{}_S\boldsymbol{\alpha}' + k_3\,{}_{SK}\boldsymbol{\alpha}\big]. \tag{14}$$

In the absence of higher-order terms (i.e., $\ell = 0$), from Eqs. (14) and (7) one obtains ${}_{SK}\mathbf{G} = \mathbf{0}$ and the higher-order balance written in terms of kinematic quantities reduces to

$$\sqrt{\frac{2}{3}}\frac{\Gamma_G S}{\mu}\frac{{}_S\mathbf{G}}{|{}_S\mathbf{G}|} = -J_e^{-1}\frac{3}{\mathrm{tr}(\bar{\mathbf{B}}_e^{-1})}\Gamma_G(\bar{\mathbf{B}}_e^{-1})'. \tag{15}$$

By taking the magnitude of this relation and combining it with definition (11), one obtains the *criterion* $S = \sigma_M$, which establishes that, in the proposed finite-deformation framework, the onset of micro-plasticity is governed by the stress $\mathbf{M}/\Gamma_G$.

Next, the m$\mathcal{M}$ theory is completed by specifying the equations governing the smooth transitions between the elastic and the plastic regimes.

2.5. Smooth elastoplastic transitions

The transition between elasticity and macro-plasticity relies on the proposal in (Hollenstein et al., 2013, 2015), such that the function Γ in (1) is given by

$$\Gamma = b_1\dot{\varepsilon}\langle y\rangle, \tag{16}$$

where $b_1 \geq 0$ is a material parameter governing the transition smoothness, $\dot{\varepsilon}$ is the effective total distortional rate

$$\dot{\varepsilon} = \sqrt{2/3}|\mathbf{D}'|, \tag{17}$$

[3] Through an initial rapid increase of size-dependent hardening, *less-than-quadratic* defect energies allow for the modeling of some strengthening (Ohno and Okumura, 2007; Bardella, 2010; Svendsen and Bargmann, 2010; Forest and Guéninchault, 2013; Bardella and Panteghini, 2015; El-Naaman et al., 2019; Kuroda and Needleman, 2023), although these potentials lead to a response that may be inadequate under non-proportional loading in polycrystal plasticity (Panteghini et al., 2019), including a change of curvature in the stress–strain curve under cyclic loading.

$$\langle x \rangle = \max(x, 0)$$

are the Macaulay brackets, and y is the yield function, which is specified as

$$y = \frac{\sigma_M}{\kappa} - 1\,, \tag{18}$$

with κ accounting for the conventional macro-plastic hardening. Its evolution equation is taken in the form

$$\dot{\kappa} = m_\kappa \Gamma(\kappa_s - \kappa)\,, \quad \kappa(0) = \kappa_0 > 0\,, \tag{19}$$

where κ_0 is the initial macro-yield stress and $m_\kappa \geq 0$ controls the rate at which κ approaches its saturated value $\kappa_s \geq \kappa_0$.

The function Γ_G that enters Eqs. (1) and (12) also governs the transition between elasticity and micro-plasticity through the introduction of the evolution equation for the micro-plasticity hardening S,

$$\dot{S} = m_S \dot{\varepsilon}\, \Gamma_G \big(\kappa - S\big)\,, \quad S(0) = S_0 > 0\,, \tag{20}$$

where S_0 is the initial micro-yield stress and $m_S \geq 0$ controls the rate at which S approaches its saturated value. It is important to highlight that this saturated value for the micro-hardening is the *current* value κ of the macro-hardening. This is consistent with the notion that the onset of micro-plasticity occurs either before or at the same stress state as macro-plasticity. Also, Eq. (20) fixes an oversight in (Rubin and Bardella, 2023), where $\dot{\varepsilon}$ is missing.

In (Rubin and Bardella, 2023), Γ_G is specified by the following function, denoted as Γ_G^{R} in this work,

$$\Gamma_G^{\mathrm{R}} = b_G \langle \frac{\sigma_M}{S} - 1 \rangle^2\,, \tag{21}$$

where R as a superscript means "reference" and the constant $b_G > 0$ controls the smoothness of the elasto–micro-plastic transition. On the basis of the argument about Eq. (15), Eq. (21) assumes that the onset of micro-plasticity occurs when $\sigma_M = S$. The exponent 2 in (21) has allowed Rubin and Bardella (2023) to obtain a convenient analytical solution for the simple shear benchmark problem under monotonic loading.

In order to model non-proportional loading, Γ_G is proposed in the modified form

$$\Gamma_G = \frac{a_G \Gamma_{\max} \overline{\Gamma}_G}{1 + a_G \overline{\Gamma}_G}\,, \quad \overline{\Gamma}_G = \max(\overline{\Gamma}_G, \Gamma_G^{\mathrm{R}})\,, \quad \overline{\Gamma}_G(t=0) = 0\,, \tag{22}$$

where $\Gamma_{\max}$ is the maximum value of Γ_G and the constant $a_G > 0$ controls the rate of increase of Γ_G. Under proportional loading, Eq. (22) specializes to the model in (Rubin and Bardella, 2023) in the limit that $a_G \to 0$ with $\Gamma_{\max} = 1/a_G$. The reason for this modification is documented in Appendix C with reference to cyclic loading.

2.6. Specialization of the theory to small deformations

In the framework of small strains and rotations from a zero-stress state in which $J_e = 1$ and $\bar{\mathbf{B}}_e = \mathbf{I}$, the total strain $\boldsymbol{\varepsilon}$ is defined in terms of the displacement field $\mathbf{u}$ as

$$\boldsymbol{\varepsilon} = \frac{1}{2}[\mathrm{grad}\,\mathbf{u} + (\mathrm{grad}\,\mathbf{u})^T]\,.$$

Also, the approximations

$$\mathbf{D}' = \dot{\boldsymbol{\varepsilon}}'\,, \quad J_e = 1 + \mathrm{tr}(\boldsymbol{\varepsilon})$$

hold for the distortional deformation rate $\mathbf{D}'$ and the elastic dilatation J_e. Moreover, by introducing the deviatoric elastic strain $\boldsymbol{\varepsilon}^{e\prime}$, one has

$$\bar{\mathbf{B}}_e' = 2\boldsymbol{\varepsilon}^{e\prime}\,, \quad \bar{\mathbf{B}}_e^{-1} = \mathbf{I} - 2\boldsymbol{\varepsilon}^{e\prime}$$

for the elastic distortional deformation $\bar{\mathbf{B}}_e'$ and $\bar{\mathbf{B}}_e^{-1}$. Note that, in this framework, the material derivative $\dot{(\,)}$ becomes equivalent to partial differentiation with respect to time and the evolution Eq. (3) for J_e is automatically satisfied.

By introducing the evolution equation

$$\dot{\mathbf{g}} = \mathbf{G}\,,$$

the second-order deviatoric tensor $\mathbf{g}$ allows the straightforward integration of Eq. (4) from a state with $\boldsymbol{\alpha} = \boldsymbol{\alpha}_0(\mathbf{x}) \equiv \mathbf{0}$ to obtain

$$\boldsymbol{\alpha} = \mathrm{curl}\,\mathbf{g}\,. \tag{23}$$

This recovers the classical expression of Nye's tensor (Nye, 1953; Kröner, 1962). Moreover, the evolution equation (1) becomes

$$\dot{\boldsymbol{\varepsilon}}^{e\prime} = \dot{\boldsymbol{\varepsilon}}' - \Gamma \boldsymbol{\varepsilon}^{e\prime} - \frac{1}{2}\Gamma_G(\dot{\mathbf{g}} + \dot{\mathbf{g}}^T)\,. \tag{24}$$

The constitutive Eqs. (13) and (14) reduce to

$$\begin{aligned} &\rho_z \psi = \frac{1}{2}k\left[\mathrm{tr}(\boldsymbol{\varepsilon})\right]^2 + \mu\, \boldsymbol{\varepsilon}^{e\prime} \cdot \boldsymbol{\varepsilon}^{e\prime} + \Psi_{\mathrm{d}}(\boldsymbol{\alpha})\,, \quad \Psi_{\mathrm{d}}(\boldsymbol{\alpha}) = \frac{1}{2}\mu \ell^2 (k_1\alpha_1 + k_2\alpha_2 + k_3\alpha_3)\,, \\ &p = -k\,\mathrm{tr}(\boldsymbol{\varepsilon})\,, \quad \mathbf{T}' = 2\mu\boldsymbol{\varepsilon}^{e\prime}\,, \quad \mathbf{M} = \Gamma_G \mathbf{T}'\,, \quad \boldsymbol{\zeta} = \mu\ell^2\left[k_1\,\mathrm{tr}(\boldsymbol{\alpha})\,\mathbf{I} + k_{2\,S}\boldsymbol{\alpha}' + k_{3\,SK}\boldsymbol{\alpha}\right], \end{aligned} \tag{25}$$

such as it is observed that $\mathbf{T}'$ and $\mathbf{M}$ differ of the factor Γ_G only, i.e.

$$\sigma_M = \sigma_e \equiv \sqrt{3/2}\,|\mathbf{T}'|\,,$$

implying that both the onsets of micro- and macro-plasticity are conveniently controlled by the equivalent von Mises stress σ_e. Also, the approximation (23) of (4) causes the defect energy $\Psi_{\rm d}(\boldsymbol{\alpha})$ to be fully reversible.

Finally, from (12), the dissipative stress becomes

$$_S\mathbf{S} = \frac{2}{3}\Gamma_G S\,\frac{_S\dot{\mathbf{g}}}{G}\,,\quad _{SK}\mathbf{S} = \chi\Gamma_G S\,\frac{_{SK}\dot{\mathbf{g}}}{G}\,,\quad G = \sqrt{\frac{2}{3}|_S\dot{\mathbf{g}}|^2 + \chi|_{SK}\dot{\mathbf{g}}|^2}\,. \tag{26}$$

Substituting (25) and (26) into (7) yields the following form of the micro-plasticity balance in terms of kinematics:

$$\ell^2\,_S(\mathrm{curl}\left[k_1\,\mathrm{tr}(\boldsymbol{\alpha})\,\mathbf{I} + k_2\,_S\boldsymbol{\alpha}' + k_3\,_{SK}\boldsymbol{\alpha}\right])' + \frac{2}{3}\frac{\Gamma_G S}{\mu}\frac{_S\dot{\mathbf{g}}}{\sqrt{\frac{2}{3}|_S\dot{\mathbf{g}}|^2 + \chi|_{SK}\dot{\mathbf{g}}|^2}} - 2\Gamma_G\boldsymbol{\varepsilon}^{e\prime} = \mathbf{0}\,, \tag{27}$$

$$\ell^2\,_{SK}(\mathrm{curl}\left[k_1\,\mathrm{tr}(\boldsymbol{\alpha})\,\mathbf{I} + k_2\,_S\boldsymbol{\alpha}' + k_3\,_{SK}\boldsymbol{\alpha}\right]) + \chi\frac{\Gamma_G S}{\mu}\frac{_{SK}\dot{\mathbf{g}}}{\sqrt{\frac{2}{3}|_S\dot{\mathbf{g}}|^2 + \chi|_{SK}\dot{\mathbf{g}}|^2}} = \mathbf{0}\,. \tag{28}$$

By using (16), (17), (19), (21), and (24), Eqs. (27)–(28) determine the micro-plasticity rate $\dot{\mathbf{g}}$.

Eqs. (27) and (28) can be specialized to recover the SGP theory of Gurtin (2004) by switching off the macro-plasticity by taking $b_1 = 0$ (implying $\Gamma = 0$ through Eq. (16)), setting $\Gamma_G = 1$, and prescribing S to be a suitable function of the accumulated micro-plasticity $\int G\mathrm{d}t$ to include some isotropic hardening.

3. Finite element implementation of the small deformation theory

3.1. Weak form of the balance equations and backward Euler time-integration for general stress states

Let $\delta a(\mathbf{x})$ represent any kinematically admissible variation of the field $a(\mathbf{x})$. The internal virtual work $\delta W_{\rm i}$ within a region Ω can be expressed as

$$\delta W_{\rm i} = \int_\Omega \left[\mathbf{T}\cdot\delta\boldsymbol{\varepsilon}^{eM} + {}_S\mathbf{S}\cdot\delta({}_S\mathbf{g}) + {}_{SK}\mathbf{S}\cdot\delta({}_{SK}\mathbf{g}) + \boldsymbol{\zeta}\cdot\delta\boldsymbol{\alpha}\right]\,\mathrm{d}V\,,$$

where $\boldsymbol{\varepsilon}^{eM} = \boldsymbol{\varepsilon}^e + \Gamma\boldsymbol{\varepsilon}^{e\prime} = \boldsymbol{\varepsilon} - \Gamma_G\,{}_S\mathbf{g}$ includes elastic and macro-plastic strains.

Considering that $\delta({}_S\mathbf{g})$ is purely deviatoric, this equation can be rewritten as

$$\delta W_{\rm i} = \int_\Omega \left[\mathbf{T}\cdot\delta\boldsymbol{\varepsilon} + \left({}_S\mathbf{S} - \Gamma_G\mathbf{T}'\right)\cdot\delta({}_S\mathbf{g}) + {}_{SK}\mathbf{S}\cdot\delta({}_{SK}\mathbf{g}) + \boldsymbol{\zeta}\cdot\delta\boldsymbol{\alpha}\right]\,\mathrm{d}V\,. \tag{29}$$

Eq. (29) can be employed to develop a 3D FE formulation for the proposed theory. This is achieved by assuming an appropriate spatial discretization for the displacement $\mathbf{u}$ and for the tensorial fields ${}_S\mathbf{g}$ and ${}_{SK}\mathbf{g}$, along with a time integration scheme, which is recommended to be the backward Euler rule. Note that the presence of the curl operator in the definition of Nye's tensor implies that the spatial discretization requires $H(\mathrm{curl})$ FEs (Rognes et al., 2010; Wieners and Wohlmuth, 2011; Panteghini and Bardella, 2018), which have been developed, mostly in the context of electromagnetism, since the pivotal contribution of Nédélec (1980). This important feature allows some of the components of $\mathbf{g}$ to admit discontinuities, depending on the boundary value problem.

To simplify the notation, all quantities are referred to the time at the end of the increment t_{n+1} unless otherwise specified, while the subscript n indicates the known values at the beginning of the time increment. Thus, at a generic time step t_{n+1}, the discretized values of the kinematic quantities $\boldsymbol{\varepsilon}$, ${}_S\mathbf{g}$, ${}_{SK}\mathbf{g}$, and $\boldsymbol{\alpha}$ at the end of the time step, as well as the time increments $\Delta\boldsymbol{\varepsilon}$, $\Delta({}_S\mathbf{g})$, $\Delta({}_{SK}\mathbf{g})$, are evaluated at any point $\mathbf{x}$ in the domain Ω.

These quantities can then be used to compute the stresses $\mathbf{T}$, $\mathbf{S}$, and $\boldsymbol{\zeta}$, as well as Γ_G through the integration of the constitutive equations. This can be achieved using a predictor–corrector approach: initially, the stresses are computed by assuming the absence of macro-plasticity, i.e., $\Gamma \equiv 0$. In this case, all quantities can be obtained by iteratively solving a nonlinear scalar equation on $\Delta\Gamma_G$. Let $\Delta\hat{\Gamma}_G$ be the value of $\Delta\Gamma_G$ in the current iteration. The micro-plasticity hardening S at the end of the increment can be computed as a function of $\Delta\hat{\Gamma}_G$ by integrating Eq. (20) using a backward Euler rule. The result is:

$$S = \frac{S_n + m_S\kappa_n\left(\Gamma_{G,n} + \Delta\hat{\Gamma}_G\right)\Delta\varepsilon}{1 + m_S\left(\Gamma_{G,n} + \Delta\hat{\Gamma}_G\right)\Delta\varepsilon}\,.$$

Assuming linear elasticity governed by the fourth-order elasticity tensor $\mathcal{L}$, the Cauchy stress $\mathbf{T}$ can be computed on the basis of Eq. (24) as

$$\mathbf{T} = \mathbf{T}_n + \mathcal{L}\left[\Delta\boldsymbol{\varepsilon} - \left(\Gamma_{G,n} + \Delta\hat{\Gamma}_G\right)\Delta({}_S\mathbf{g})\right]\,.$$

The incremental form of (22) is

$$\dot{\Gamma}_G = \frac{a_G\Gamma_{\max}\dot{\overline{\Gamma}}_G}{(1 + a_G\overline{\Gamma}_G)^2}\,,\quad \dot{\overline{\Gamma}}_G = \langle\dot{\Gamma}_G^{\rm R}\rangle \equiv 2b_G\langle\frac{\sigma_e}{S} - 1\rangle\langle\frac{\dot{\sigma}_e}{S}\rangle\,, \tag{30}$$

where Eq. (21) has been used in the last equivalence and $\sigma_M \equiv \sigma_e$ for small deformations. Eq. (30) can be discretized as

$$\Delta\Gamma_G = \frac{a_G \Gamma_{\max} \Delta\overline{\Gamma}_G}{\left[1 + a_G\left(\overline{\Gamma}_{G,n} + \Delta\overline{\Gamma}_G\right)\right]^2}, \quad \Delta\overline{\Gamma}_G = \langle \Delta\Gamma_G^{\mathrm{R}} \rangle \equiv 2 b_G \langle \frac{\sigma_e}{S} - 1 \rangle \langle \frac{\Delta\sigma_e}{S} \rangle, \tag{31}$$

where $\Delta\sigma_e = \sigma_e - \sigma_{e,n}$. Now, $\Delta\hat{\Gamma}_G$ can be iteratively determined by simply solving the nonlinear algebraic equation

$$\Delta\Gamma_G - \Delta\hat{\Gamma}_G = 0. \tag{32}$$

Once $\Delta\Gamma_G$, S, and $\mathbf{T}$ have been computed, one can verify if the initial assumption of $\Gamma = 0$ is correct, i.e., if no macro-plasticity occurs in the current step. This can be done by computing the trial values y^* and Γ^* of the yield function (18) and of Γ as

$$y^* = \frac{\sigma_e}{\kappa_n} - 1, \quad \Gamma^* = b_1 \frac{\Delta\varepsilon}{\Delta t} \langle y^* \rangle.$$

If $\Gamma^* = 0$, no macro-plasticity occurs and the obtained solution is acceptable. Otherwise, $\Gamma \neq 0$ and a different solution must be computed. In this case, all quantities can be obtained by iteratively solving a 2×2 nonlinear algebraic system of equations for $\Delta\Gamma_G$ and y. Let $\Delta\hat{\Gamma}_G$ and $\hat{y}$ be the values of $\Delta\Gamma_G$ and y at the current iteration. Observing that from Eq. (16) one obtains

$$\Gamma \Delta t = \left(b_1 \Delta\varepsilon\right) \hat{y},$$

the macro-plasticity hardening κ at the end of the increment can be computed as a function of $\hat{y}$ by integrating Eq. (19). The result is

$$\kappa = \frac{k_n + m_\kappa \kappa_s \left(b_1 \Delta\varepsilon\right) \hat{y}}{1 + m_\kappa \left(b_1 \Delta\varepsilon\right) \hat{y}}$$

The micro-plasticity hardening S, which also depends on κ, is now a function of both $\Delta\hat{\Gamma}_G$ and $\hat{y}$. By integrating Eq. (20), one obtains

$$S = \frac{S_n + m_S \kappa \left(\Gamma_{G,n} + \Delta\hat{\Gamma}_G\right) \Delta\varepsilon}{1 + m_S \left(\Gamma_{G,n} + \Delta\hat{\Gamma}_G\right) \Delta\varepsilon}$$

The Cauchy stress $\mathbf{T}$ can be computed by assuming linear elasticity and integrating the elastic strain rate from Eq. (24). The result is

$$\mathbf{T} = \frac{1}{1 + \left(b_1 \Delta\varepsilon\right) \hat{y}} \left[\mathbf{T}'_n + \mathcal{L} \Delta\boldsymbol{\varepsilon}' - \left(\Gamma_{G,n} + \Delta\hat{\Gamma}_G\right) \Delta({}_S\mathbf{g})\right] + \mathcal{L}\left(\frac{\mathrm{tr}\,\boldsymbol{\varepsilon}}{3}\mathbf{I}\right)$$

Now, $\Delta\hat{\Gamma}_G$ and $\hat{y}$ can be iteratively determined by simply imposing

$$\begin{cases} \dfrac{\sigma_e}{\kappa} - 1 - \hat{y} = 0 \\ \Delta\Gamma_G - \Delta\hat{\Gamma}_G = 0 \end{cases} \tag{33}$$

where $\Delta\Gamma_G$ is obtained from Eq. (31). Once Γ, Γ_G, S, κ, and $\mathbf{T}$ are determined, the dissipative stress $\mathbf{S}$ can be computed. This can be done by modifying Eq. (26) with the introduction of a *suitable* viscoplastic function $V(G)$. This allows the numerical algorithm to converge when the effective micro-plastic increment $\Delta G = G \Delta t$ is very small, for which $V(G)$ is conveniently assumed to be linear in G. The result is

$${}_S\mathbf{S} = \frac{2}{3} \Gamma_G V(G) S \frac{\Delta({}_S\mathbf{g})}{\Delta G}, \quad {}_{SK}\mathbf{S} = \chi \Gamma_G V(G) S \frac{\Delta({}_{SK}\mathbf{g})}{\Delta G}, \quad \Delta G = \sqrt{\frac{2}{3} |\Delta({}_S\mathbf{g})|^2 + \chi |\Delta({}_{SK}\mathbf{g})|^2},$$

where (Bardella and Panteghini, 2015; Panteghini and Bardella, 2016)

$$V(G) = \begin{cases} \dfrac{G}{2\dot{\varepsilon}_0} & \text{if } \dfrac{G}{\dot{\varepsilon}_0} \leq 1 \\ 1 - \dfrac{1}{2}\dfrac{\dot{\varepsilon}_0}{G} & \text{if } \dfrac{G}{\dot{\varepsilon}_0} > 1 \end{cases} \tag{34}$$

with $\dot{\varepsilon}_0$ denoting a rate-sensitivity material parameter that, in this investigation, is set to a very low value to obtain a material response that is substantially rate-independent. Specifically, for all the analyses in Section 4,

$$\dot{\varepsilon}_0 = 5 \cdot 10^{-6}\ \mathrm{s}^{-1} \tag{35}$$

and each loading ramp from zero load to its maximum applied value (or *viceversa*) lasts 1 s.

Finally, the defect stress $\boldsymbol{\zeta}$ can be computed as a function of $\boldsymbol{\alpha}$ at the end of the increment by using the third of Eqs. (25).

Although in the following focus is on an *ad hoc* FE implementation for the simple shear problem, it is remarked that the foregoing algorithm holds for any stress state, so it can be used to implement 2D and 3D continuum $H(\mathrm{curl})$ FEs. For small deformations, the implementation of the m$\mathcal{M}$ theory in 2D $H(\mathrm{curl})$ FEs requires relatively limited modifications with respect to the implementation in (Panteghini and Bardella, 2018) of the SGP of Gurtin (2004).

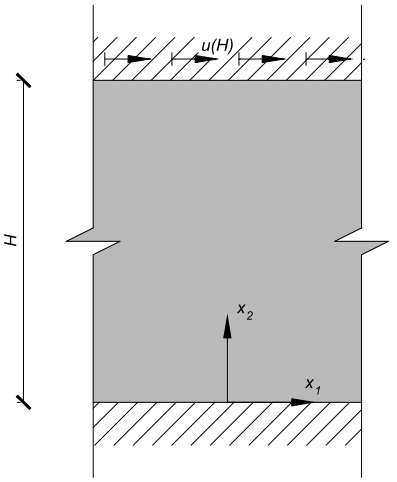

Fig. 1. Schematic of the simple shear problem.

3.2. Spatial discretization for the simple shear problem

3.2.1. The constrained simple shear problem

This work focuses on the simple shear of a strip of thickness H in the $\mathbf{e}_1$-$\mathbf{e}_2$ plane of a fixed orthonormal triad $\mathbf{e}_i$. It is assumed that body forces and acceleration are negligible and that the strip is unbounded along the $\mathbf{e}_1$ and $\mathbf{e}_3$ directions, such that the displacement u_1 depends on (x_2, t) only. As sketched in Fig. 1, the strip side at $x_2 = 0$ is clamped while the top side $x_2 = H$ is subjected to a velocity $\dot{u}_1(H, t)$ along the $\mathbf{e}_1$ direction. With these assumptions, the elastic deformation and the macro-plastic deformation rate are spatially uniform.

To obtain semi-analytical results for this problem under monotonic loading, Rubin and Bardella (2023) have further assumed $m_\kappa = m_S = 0$ in (19) and (20), such that $S = S_0$ and $\kappa = \kappa_0$ are constants. Here, this assumption is removed and non-proportional loading is studied as well.

The sole non-vanishing components of the fields u_i, ε_{ij}, ε^e_{ij}, g_{ij}, α_{ij}, ζ_{ij} are

$$u_1\,,\quad \varepsilon_{12}\,,\quad \varepsilon^e_{12}\,,\quad g_{12}\,,\quad g_{21}\,,\quad \alpha_{23} = -g_{21,2}\,,\quad \zeta_{23} = -\tilde{\mu}\ell^2 g_{21,2}\,,\quad \zeta_{32} = -\frac{1}{2}\mu(k_2 - k_3)\ell^2 g_{21,2}\,, \tag{36}$$

where

$$\tilde{\mu} = \frac{1}{2}\mu(k_2 + k_3) \tag{37}$$

and the expression for ζ_{32} in Eq. (36) corrects a typographical error in (Rubin and Bardella, 2023).

It then turns out that

$$\begin{aligned}
&\dot{\varepsilon}_{12} = \frac{1}{2}\dot{u}_{1,2}\,,\quad \dot{\varepsilon} = \frac{1}{\sqrt{3}}|\dot{u}_{1,2}|\,,\quad |\mathrm{curl}(\boldsymbol{\alpha})| = |g_{21,22}|\,,\quad {}_S(\mathrm{curl}\boldsymbol{\zeta})'_{12} = -{}_SK(\mathrm{curl}\boldsymbol{\zeta})_{12} = -\frac{1}{2}\tilde{\mu}\ell^2 g_{21,22}\,,\\
&T_{12} = 2\mu\varepsilon^e_{12}\,,\quad M_{12} = \Gamma_G T_{12}\,,\quad \sigma_e = \sqrt{3}|T_{12}|\,,\quad {}_SS_{12} = \frac{\Gamma_G S}{3}\Big(\frac{\dot{g}_{12} + \dot{g}_{21}}{G}\Big)\,,\quad {}_SKS_{12} = \frac{\chi\Gamma_G S}{2}\Big(\frac{\dot{g}_{12} - \dot{g}_{21}}{G}\Big)\,,\\
&\Gamma_G S = \sqrt{3({}_SS_{12})^2 + \frac{2}{\chi}({}_SKS_{12})^2}\,,\quad G = \sqrt{\frac{1}{3}(\dot{g}_{12} + \dot{g}_{21})^2 + \frac{\chi}{2}(\dot{g}_{12} - \dot{g}_{21})^2}\,.
\end{aligned} \tag{38}$$

In particular, ζ_{32} does not enter the higher-order balance equations (7), which reduce to

$${}_SS_{12} = T_{12} - \frac{1}{2}\zeta_{23,2}\,,\quad {}_SKS_{12} = \frac{1}{2}\zeta_{23,2}\,. \tag{39}$$

Furthermore, the microhard boundary conditions (8) are specified by

$$g_{21}(0, t) = g_{21}(H, t) = 0\,. \tag{40}$$

In order to display the stress–strain response, it is convenient to define the "applied engineering shear strain" as

$$\frac{u(H)}{H} = \frac{1}{H}\int \dot{u}_1(H, t)\,\mathrm{d}t\,,$$

that is, the (through-the-thickness) average of the displacement gradient. Note that, for convenience, the dependence of $u(H)$ on t is dropped here and henceforth.

3.2.2. Finite element discretization

Under the foregoing assumptions, this boundary value problem is spatially one-dimensional, such that a 1D FE formulation can be conveniently pursued and, in the following, the notation is simplified by using $u \equiv u_1$.

For a strip of unitary out-of-plane width, the internal virtual work in Eq. (29) can be specialized to

$$\delta W_{\rm i} = \int_0^H \left[2T_{12}\delta\varepsilon_{12} + \left({}_S S_{12} - \Gamma_G T_{12}\right)\delta(g_{12}+g_{21}) + {}_{SK}S_{12}\delta(g_{12}-g_{21}) + \zeta_{23}\delta\alpha_{23}\right]\,{\rm d}x_2\,. \tag{41}$$

Following the standard FE method, a spatial discretization is adopted both for the displacement field u and for the micro-plasticity fields g_{12} and g_{21}. The values of these fields at FE nodes are contained in the vectors $\hat{\mathbf{u}}$, $\hat{\mathbf{g}}_{12}$, and $\hat{\mathbf{g}}_{21}$ respectively. Each vector has $\hat{n}$ components, where $\hat{n}$ is the total number of nodes of each FE. This discretization is based on the shape functions $N^{(i)}(\xi)$, where $i = 1,\dots,\hat{n}$ and $\xi \in [-1,1]$ denotes the intrinsic parent element coordinate. The same shape functions are used for all fields and isoparametric FEs are adopted. Therefore, the coordinate $x_2(\xi)$ is expressed as

$$x_2(\xi) = \sum_{i=1}^{\hat{n}} x_2^{(i)} N^{(i)}(\xi)\,,$$

where $x_2^{(i)}$ are the nodal values of the coordinate. Hence, it follows that

$$\varepsilon_{12}(\xi) = \frac{1}{2}\mathbf{B}(\xi)\,\hat{\mathbf{u}}\,,\quad g_{12}(\xi) = \mathbf{N}(\xi)\,\hat{\mathbf{g}}_{12}\,,\quad g_{21}(\xi) = \mathbf{N}(\xi)\,\hat{\mathbf{g}}_{21}\,,\quad \alpha_{23}(\xi) = \mathbf{C}(\xi)\,\hat{\mathbf{g}}_{21}\,, \tag{42}$$

where

$$\mathbf{B}(\xi) = \left[\frac{dN^{(1)}}{dx_2}\;\dots\;\frac{dN^{(\hat{n})}}{dx_2}\right],\quad \mathbf{N}(\xi) = \left[N^{(1)}\;\dots\;N^{(\hat{n})}\right],\quad \mathbf{C}(\xi) = -\left[\frac{dN^{(1)}}{dx_2}\;\dots\;\frac{dN^{(\hat{n})}}{dx_2}\right].$$

Substituting Eq. (42) into (41) gives the discretized virtual work for the simple shear problem, in the form

$$\delta W_{\rm i} = \int_0^H \left\{\left(T_{12}\mathbf{B}\right)\delta\hat{\mathbf{u}} + \left[\left({}_S S_{12} + {}_{SK}S_{12} - \Gamma_G T_{12}\right)\mathbf{N}\right]\delta\hat{\mathbf{g}}_{12} + \left[\left({}_S S_{12} - {}_{SK}S_{12} - \Gamma_G T_{12}\right)\mathbf{N} + \zeta_{23}\mathbf{C}\right]\delta\hat{\mathbf{g}}_{21}\right\}\,{\rm d}x_2\,.$$

Differentiating this expression with respect to the variations of the nodal variables $\hat{\mathbf{u}}$, $\hat{\mathbf{g}}_{12}$, and $\hat{\mathbf{g}}_{21}$ gives the vectors of the internal nodal forces, as

$$\begin{aligned}
\mathbf{F}^{\rm int}_{u} &= \int_0^H \mathbf{B}^T T_{12}\,{\rm d}x_2\,,\\
\mathbf{F}^{\rm int}_{g_{12}} &= \int_0^H \mathbf{N}^T\left({}_S S_{12} + {}_{SK}S_{12} - \Gamma_G T_{12}\right)\,{\rm d}x_2\,,\\
\mathbf{F}^{\rm int}_{g_{21}} &= \int_0^H \left[\mathbf{N}^T\left({}_S S_{12} - {}_{SK}S_{12} - \Gamma_G T_{12}\right) + \mathbf{C}^T\zeta_{23}\right]\,{\rm d}x_2\,.
\end{aligned} \tag{43}$$

Standard details on the transformation between real and intrinsic coordinate systems are omitted for the sake of brevity. The consistent stiffness matrix $\mathbf{K}$, which is provided in Appendix A, is essential to complete the FE algorithm and ensure second-order convergence of the structural Newton–Raphson scheme.

The foregoing FE algorithm has been implemented as a user element subroutine (`uel`) in the commercial FE code ABAQUS (Dassault Systèmes, 2013). All the FE results discussed in the following examples have been obtained by discretizing the strip with a uniform mesh of 250 fully-integrated quadratic (3-noded) elements. This spatial discretization has been selected on the basis of a convergence study.

4. Examples of small deformation simple shear

In the following examples the constants χ, k_2, k_3 are specified by

$$\chi = 10.\,,\quad k_2 = k_3 = 10.$$

and, in Sections 4.1 and 4.2, all conventional stresses are normalized by the shear modulus μ. Also, different sets of the other material parameters, such as those provided in Tables 1 and 2, will be used to study the model response. For brevity, the model that includes both micro-plasticity and macro-plasticity is denoted as the m$\mathcal{M}$-model; the model that includes macro-plasticity only is denotes as the $\mathcal{M}$-model; and the model that includes micro-plasticity only is denoted as the m-model.

The value $\chi = 10$ allows a large increase of the shear stress in the strip after first yielding in the m-model without hardening. Such an increase in the m-model is expected to depend on χ because the maximum σ_e in the model in (Rubin and Bardella, 2023), where $\Gamma_G = \Gamma_G^{\rm R}$, is given by the saturation stress

$$\sigma_s^{\rm micro} = S_0\sqrt{1+\frac{3\chi}{2}}\,, \tag{44}$$

which, correspondingly, is the maximum possible equivalent stress predicted by the SGP of Gurtin (2004) applied to the constrained simple shear without hardening (Panteghini and Bardella, 2018).

To study the predicted size-effects, results are presented for different values of the non-dimensional strip thickness

$$r = \frac{H}{\ell}\,.$$

Since $\tilde{\mu}$ in (37) depends on $(k_2 + k_3)$, there is no loss in generality in specifying $k_2 = k_3$; by the way, this choice leads, through the last relation in Eq. (36), to vanishing ζ_{32}, which has no influence on the response because α_{23} is the sole non-vanishing Nye tensor component in this simple shear problem. Also, the chosen value for $k_2 = k_3$ is unimportant as it is, again, a redundant parameter because it always multiplies ℓ^2. Also, when studying the scaling law for the *apparent yield stress* σ_Y with respect to the strip size H (in Section 4.2), the chosen value of $k_2 = k_3$ has an impact only on the range of H, not on the slope of the curve in the $(\log \sigma_Y, \log H)$ graph, which is one goal of that study.

The validation of the FE implementation is provided in Appendix B and the reason to modify the form of Γ_G in (22), which is always used in the following, is documented and discussed in Appendix C. Before delving into the details of the new results, a fundamental feature of the behavior predicted by the m$\mathcal{M}$ theory is recalled and discussed.

The behavior predicted by the m$\mathcal{M}$-model might at first seem strange since the response of the largest sample is controlled by micro-plasticity and the response of the smallest specimen is controlled by macro-plasticity. In particular, this implies that the strongest response predicted by the m-model (that is, in the absence of macro-plasticity) tends towards linear elasticity. This use of the terminology "micro- and macro-plasticity" is consistent with three distinct literature sources. First, the generalized continua developed since Cosserat and Cosserat (1909), where the micro- and macro-fields separately contribute, in the same tensorial equation, to the gradient of the displacement field (see, e.g., Mindlin, 1964; Maugin, 1979; Green and Naghdi, 1995; Eringen, 1999; Forest and Sievert, 2003; Forest, 2008; Hirschberger and Steinmann, 2009; Forest, 2020; Bertram, 2023 and references therein). Second, the experimental evidence referred to as "micro-plasticity" in (Maaß and Derlet, 2018, and references therein), where focus is on tiny and irreversible deformations measured before the onset of *macroscopic* yielding, referred to as *apparent* yielding in this investigation: in the m$\mathcal{M}$ theory this can be incorporated by imposing $S_0 < \kappa_0$, such that micro-plasticity develops at a stress level lower than that triggering macro-plasticity. Third, the body of work on SGP following Gurtin, where the fields defining the higher-order part of a SGP theory are denoted through the prefix "micro". With respect to this literature, it is however important to highlight the stark difference of the terminology adopted here, where macro-plasticity turns out to govern the strongest material response. Hence, the proposed model might conveniently be recasted into a rheological model where a single elastic spring and two nonlinear inelastic dashpots due to micro- and macro-plasticity are connected in series. The resistance to micro-plastic flow increases with decrease in the size of the specimen. Consequently, for large specimens the "micro-dashpot" is weaker than the "macro-dashpot", so the former dominates the response, while the opposite behavior is observed for small specimens.

In particular, the fact that micro-plasticity governs the response of large samples works only if the micro-plastic components can assume profiles that are expected in conventional plasticity. This is not the case if micro-hardening is neglected when plastic flow gradients influence the material response exclusively through a quadratic defect energy. In fact, in constrained simple shear, the absence of micro-hardening leads to a parabolic profile of the micro-plastic strain (Rubin and Bardella, 2023), and, of course, this mirrors the behavior of the plastic fields predicted by higher-order SGP models applied to the same benchmark problem (see Anand et al., 2005, for a general one-dimensional SGP theory and Panteghini and Bardella, 2018, for the SGP theory of Gurtin, 2004). In constrained simple shear, a plastic field profile that is quadratic irrespective of the sample size is unphysical because of the expectation, suggested by the behavior of GNDs piling up at the strip edges, that there must be boundary layers of amplitude independent of the strip height, while there should be a strip middle region subject to about uniform plasticity whose size is proportional to the strip height. It is well-known from the literature that this can be achieved by adding some hardening. For instance, in the case of linear hardening, the higher-order plastic field is governed by hyperbolic functions that allow mimicking the expected behavior (see, e.g., Bittencourt et al., 2003). It is also remarked that, while g_{21} must always vanish at the boundary if microhard boundary conditions (40) are prescribed, introduction of hardening may allow g_{12} to be non-zero at the boundary (Panteghini and Bardella, 2018), thus further improving the range of possible responses.

The foregoing behavior is illustrated here by referring to the set of parameter V_3 in Table 1, as adopted in (Rubin and Bardella, 2023) to describe the response of the m-model. Fig. 2 compares, for different strip heights, the stress–strain curves and the normalized g_{12} and g_{21} profiles obtained with the sets of parameters V_3 and G_1, the latter also reported in Table 1 and selected to obtain a model close to that of Gurtin (2004) with linear hardening. Note that by decreasing r from 1000 to 1 the amplitudes of g_{12} and g_{21} diminish drastically; this cannot be seen in Fig. 2 because of the adopted normalization, aiming at better comparing the shapes of the obtained profiles. As recorded in the last row of Table 1, these responses are derived by using $\Gamma_G = \Gamma_G^{\mathrm{R}}$ in Eq. (21); by following the comment below Eq. (22), this is achieved in the FE code by setting $a_G = 0.01$ and $\Gamma_{\max} = 100$. Moreover, the value of m_s in the set G_1 is specified to be relatively large to enhance the initial micro-hardening. More importantly, in G_1 the parameter b_G is taken to be very large to minimize the overstress in the micro-hardening, as the overstress would tend to eliminate the boundary layers by smoothing them out all along the strip height even for large strip heights [almost as in the response of perfect micro-plasticity with overstress (V_3 in Table 1)]. This influence of the overstress on the size-dependent response is a novel aspect of detail of this investigation.

It is further remarked that the nonlinear behavior after yielding in the stress–strain curve for the set V_3 with $r = 1$ in Fig. 2a has to be ascribed to the dissipation due to the plastic spin rate. This is in fact the way the maximum stress value in Eq. (44) is approached. It should be noted that, when applied to the constrained simple shear problem modeled by using perfect plasticity and a quadratic defect energy, higher-order SGP theories neglecting the plastic spin (such as those of Gudmundson, 2004, and Gurtin and Anand, 2005) lead to a single model that can be obtained from the model of Gurtin (2004) by taking the limit for $\chi \to \infty$. In this case, the maximum Cauchy stress that the strip can experience is unbounded and, after yielding, the stress–strain curve remains linear, being characterized by a hardening slope which is size-dependent.

It is additionally noted that, for this benchmark problem, assuming $\chi = 0$ in the SGP of Gurtin (2004) leads to size-independent conventional plasticity, whose stress–strain curve is similar to that in Fig. 2a for the set V_3 with $r = 1000$. This is because, from the absence of dissipation due to the plastic spin rate, it follows that the plastic spin attains a profile that minimizes the defect energy.

Table 1
List of parameters for different material sets V_i adopted in (Rubin and Bardella, 2023) and G_1. The sets V_i are used in Appendix B for verification of the FE code accuracy. The parameters that have been changed in V_2, V_3, and G_1 relative to the reference parameters in V_1 are highlighted in red.

Variable	V_1	V_2	V_3	G_1
b_1	500.	500.	0.	0.
b_G	10.	0.	10.	50000.
κ_0	0.01μ	0.01μ	0.01μ	0.04μ
κ_s	0.01μ	0.01μ	0.01μ	0.04μ
m_κ	0.	0.	0.	0.
S_0	0.01μ	0.01μ	0.01μ	0.01μ
m_S	0.	0.	0.	50.
Γ_G	Γ_G^R	Γ_G^R	Γ_G^R	Γ_G^R

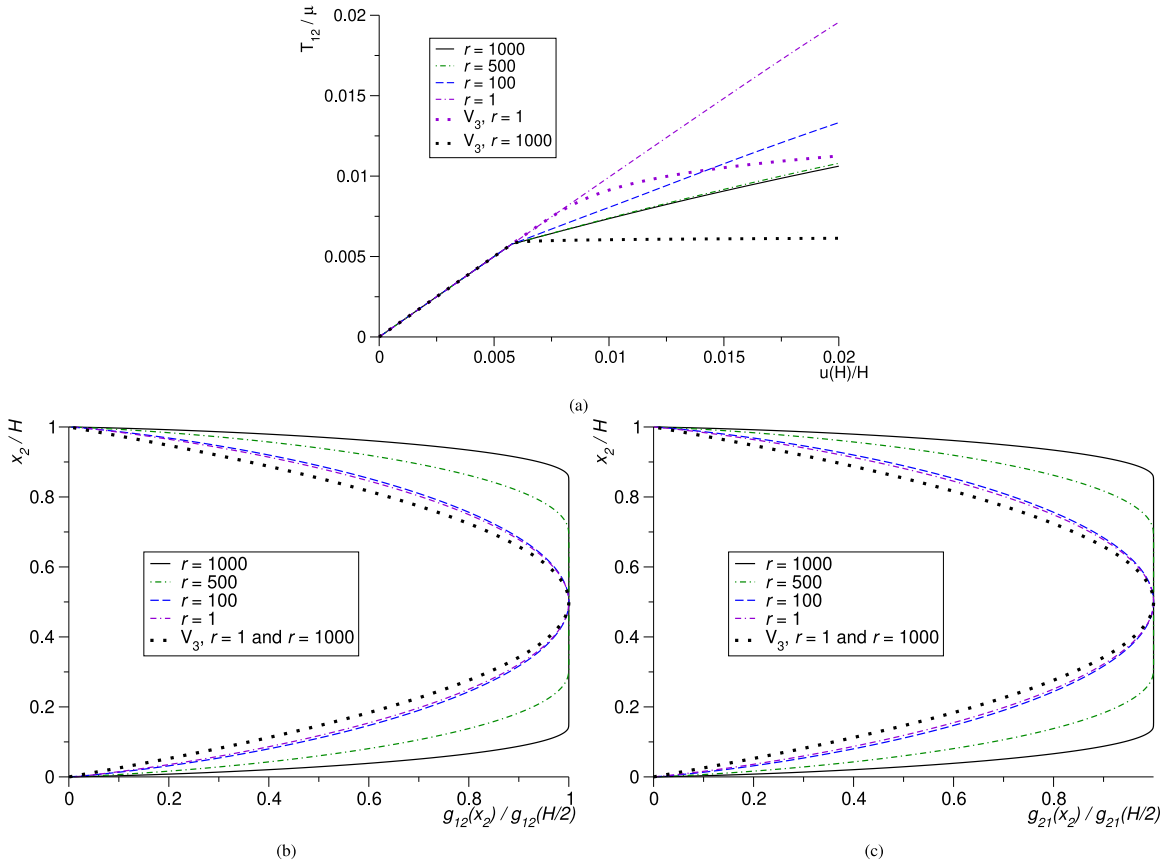

Fig. 2. Influence of the size on the elasto–micro-plastic response at $u(H)/H = 0.02$ for the m-model without overstress (G_1 in Table 1): (a) stress–strain curves; (b) profiles of the normalized g_{12} micro-plastic field; (c) profiles of the normalized g_{21} micro-plastic field. The case of perfect micro-plasticity with overstress (V_3 in Table 1) is included for comparison. The values of $g_{21}(H/2)$ are 7.34×10^{-5}, 3.52×10^{-3}, 6.74×10^{-3}, 6.44×10^{-3} for $r = 1$, 100, 500, 1000, respectively, and they are very close to the values of $g_{12}(H/2)$ because in the middle of the strip the plastic spin rate becomes negligible with respect to the plastic strain rate, mostly at large H.

As it can be easily seen from Eqs. (36), (38), (39), and (40), in the m-model applied to constrained simple shear, this minimization implies $g_{21} = 0$, i.e. uniform micro-plastic strain and micro-plastic spin of equal magnitude.

The final result of the analysis illustrated with Fig. 2 is that in the case of perfect micro-plasticity the normalized profiles of g_{12} and g_{21} are independent of r, being always quadratic, while the addition of micro-hardening allows the prediction of the boundary layers in relatively large strips and, for very large strips, the tendency to conventional plasticity is recovered. In spite of this result, it is pointed out that the m$\mathcal{M}$ theory is developed to be used, as presented next, when both micro- and macro-plasticity are active, as it is their non-trivial interaction that provides benefits in modeling the response of metals in the size range where GNDs influence the overall response.

Table 2
List of parameters for different material sets. The parameters highlighted in red are those that change relative to the reference parameters in M_4.

Variable	M_1^{R}	M_1	M_2	M_3	M_4	M_5	M_6	M_7	M_8	M_9
b_1	500.	500.	500.	0.	500.	500.	0.	500.	5000.	500.
b_G	10.	10.	0.	10.	10.	0.	10.	10.	10.	10.
κ_0	0.02μ	0.02μ	0.02μ	0.02μ	0.02μ	0.02μ	0.02μ	0.01μ	0.02μ	0.02μ
κ_s	0.04μ	0.04μ	0.04μ	0.04μ	0.04μ	0.04μ	0.04μ	0.04μ	0.04μ	0.04μ
m_κ	0.	0.	0.	0.	0.1	0.1	0.1	0.1	0.1	0.1
S_0	0.01μ	0.01μ	0.01μ	0.01μ	0.01μ	0.01μ	0.01μ	0.01μ	0.01μ	0.01μ
m_S	0.	0.	0.	0.	20.	20.	20.	20.	20.	20.
Γ_G	Γ_G^{R}	–	–	–	–	–	–	–	–	–
$\Gamma_{\max}$	–	1.5	1.5	1.5	1.5	1.5	1.5	1.5	1.5	3.
a_G	–	5.	5.	5.	5.	5.	5.	5.	5.	5.

4.1. Cyclic loading

All the results in this section are obtained and displayed for four full cycles of applied engineering shear strain $u(H)/H$ ranging from 0.02 to −0.02, which are imposed after a loading ramp where $u(H)/H$ reaches the value 0.02 for the first time. Depending on the adopted material parameters for the micro- and macro-hardening and also on the material length scale ℓ and on the parameter χ governing the dissipation due to the plastic spin rate, different cycles may or may not be easily distinguished in the stress–strain curves displayed in the following. In fact, these parameters control the number of cycles needed to obtained a stabilized response (for instance corresponding to saturation of the hardening variables) for a given amplitude of the cycle in the plasticity regime.

Fig. 3 presents results in the absence of hardening predicted by: the m$\mathcal{M}$-model (M_1 in Table 2), the m-model (M_3 in Table 2), and the model of Gurtin (2004) as implemented in (Panteghini and Bardella, 2018).[4] Fig. 3a,b include predictions of the $\mathcal{M}$-model (M_2 in Table 2) for comparison. From these figures it can be seen that the predictions of the m-model and the Gurtin model are similar as expected (the sole difference between these two models, in the absence of hardening, is due to the Γ_G function entering the present theory), while the predictions of the m$\mathcal{M}$-model show nonlinear coupling between micro- and macro-plasticity that is explored in the following examples which include micro- and macro-hardening.

Fig. 4 presents results with hardening for three values of the normalized thickness r predicted by: the m$\mathcal{M}$-model (M_4 in Table 2), the $\mathcal{M}$-model (M_5 in Table 2), and the m-model (M_6 in Table 2). In particular, it can be seen from Fig. 4c that for the smallest specimen ($r = 1$) the m-model hardens quickly to cause nearly elastic response for the imposed strain range. This behavior is bounded by the elasto–macro-plastic response in the m$\mathcal{M}$-model, as displayed in Fig. 4a. In the following, only results obtained with the complete m$\mathcal{M}$-model will be discussed.

Fig. 5 shows the influence of changing the value of the onset of macro-yielding κ_0 for three values of the normalized thickness r. Specifically, predictions of the m$\mathcal{M}$-model with hardening for $\kappa_0 = 0.02\mu$ (M_4 in Table 2) and for $\kappa_0 = 0.01\mu$ (M_7 in Table 2) are compared. Note that the material set M_7 is a "limit set" because $S_0 = 0.01\mu = \kappa_0$, that is, the onsets of micro- and macro-plasticity coincide; this causes the lack of hardening exhibited by this material at large r in Fig. 5c. Specifically, micro-plasticity develops without the need of appreciably increasing the stress because the higher-order stress ζ_{23} gives a negligible contribution in the higher-order balance in Eq. (39). More in general, from Fig. 5 it can be seen that κ_0 has a large effect on the response.

Fig. 6 shows the influence of changing the value of b_1 for three values of the normalized thickness r. Specifically, predictions of the m$\mathcal{M}$-model with hardening for $b_1 = 500$ (M_4 in Table 2) and for $b_1 = 5000$ (M_8 in Table 2) are compared. From this figure it can be seen that increasing the value of b_1 causes a sharper elastoplastic transition, and, of course, this behavior is observed especially for the small specimens, where macro-plasticity dominates.

Fig. 7 shows responses for three values of the normalized thickness r to study the influence of changing the value of $\Gamma_{\max}$, that is the saturation value of the Γ_G function proposed in Eq. (22). Specifically, predictions of the m$\mathcal{M}$-model with hardening for $\Gamma_{\max} = 1.5$ (M_4 in Table 2) and for $\Gamma_{\max} = 3.0$ (M_9 in Table 2) are compared. From this figure it can be seen that this change in $\Gamma_{\max}$ has little effect on the predictions of the largest ($r = 100$) and smallest ($r = 1$) specimens, while it has an observable effect on the behavior of the specimen with intermediate size ($r = 5$).

4.2. Scaling of the apparent yield stress

By following the pioneering investigations of Hall (1951) and Petch (1953), in the literature, see e.g. Kuroda et al. (2021) and references therein, whatever *apparent* yield stress σ_Y is defined, it is in most cases assumed that it scales with the specimen size, H, through a power-law. Here, σ_Y, which is the value of σ_e at apparent yield, is defined by the "0.2% offset rule", which identifies the apparent yield stress as the value of stress at the intersection of the stress–strain curve and the linear elastic unloading line that

[4] Note that to compare the m-model with the model of Gurtin (2004) one has to set the length scale parameter in the latter, denoted as ℓ_{Gur}, by equating $\mu\ell^2(k_2 + k_3)/2$, weighing the defect energy in the m-model, with $\mu\ell_{\mathrm{Gur}}^2$, weighing the defect energy in the Gurtin model.

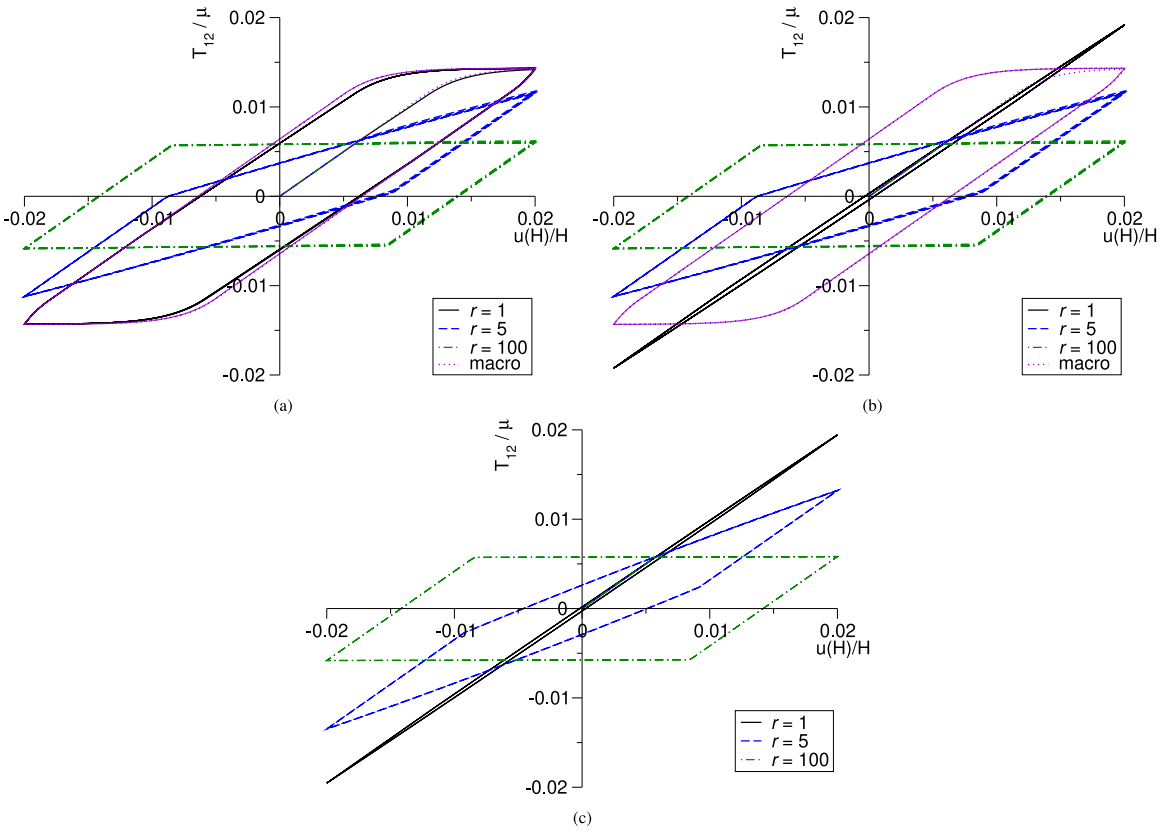

Fig. 3. Cyclic loading without hardening. Predictions of: (a) the m$\mathcal{M}$-model (M_1 in Table 2); (b) the m-model (M_3 in Table 2); and (c) the model of with Gurtin (2004) without hardening. The $\mathcal{M}$-model (M_2 in Table 2) is included for comparison between (a) and (b).

starts at 0.2% engineering shear strain. Specifically, consider the expression between the normalized yield stress and the normalized specimen size

$$\frac{\sigma_Y}{\mu} = a\left(\frac{H}{\ell}\right)^b \equiv a r^b\,, \tag{45}$$

where a and b are non-dimensional constants. It is assumed that Eq. (45) holds within different ranges of specimen size by adequately setting the coefficients a and b for each range. For instance, at large size $b \to 0$ and $a\mu$ becomes the apparent yield stress of a large sample. Importantly, Dunstan and Bushby (2014) demonstrate that b does not have a universal value, as it is instead a material parameter that should be calibrated for each metal.

Taking the logarithm of Eq. (45) yields two forms of the same expression

$$\log\frac{\sigma_Y}{\mu a} = b\log\frac{H}{\ell} \equiv b\log r \quad \text{and} \quad \log(\sigma_Y) = c + b\log(H)\,, \quad c = \log\frac{\mu a}{\ell^b}\,,$$

either of which can be used to determine the value of the slope b from a curve obtained on a log–log plot. Some investigators (see, e.g., Cruzado et al., 2024) propose to suitably divide the available data in two sets, one for small sizes and one for larger sizes, over which determining two values of b through two linear regressions on the log–log plot. This strategy is followed here as well by using the ranges $r \in [1, 10]$ and $r \in [10, 1000]$.

Fig. 8 shows the normalized yield stress versus the ratio $r = H/\ell$ on a log–log plot obtained by considering monotonic loading of the m$\mathcal{M}$-model for the sets of parameters M_4, M_7, M_8, M_9 in Table 2. The predictions of M_4 are used as a reference. Consequently, the results of this reference are compared with those of M_7, M_8, and M_9, examining, respectively, the influence of changing κ_0, b_1, and $\Gamma_{\max}$. Also, Table 3 records the obtained values of the exponent b. From these results it can be seen that changing b_1 has no influence on the onset of plasticity if r is not too small. This is consistent with Fig. 6b and c, showing that the onset of plasticity for the material M_8 is controlled by micro-plasticity since macro-plasticity initiates at a higher stress level for this material set, except that for very small r (see Fig. 6a) the micro-plastic behavior is almost linear elastic up to the onset of macro-plasticity, whose smooth transition then affects σ_Y. The main result from Fig. 8 is that both changing κ_0 and changing $\Gamma_{\max}$ have significant influences on the yield stress for small specimens. This is a kind of obvious result for κ_0, given that the ratio κ_0/S_0 is expected to be significant for the determination of σ_Y. Although the influence of $\Gamma_{\max}$ on the apparent yield stress is less straightforward, it confirms the result in Fig. 7b for $r = 5$.

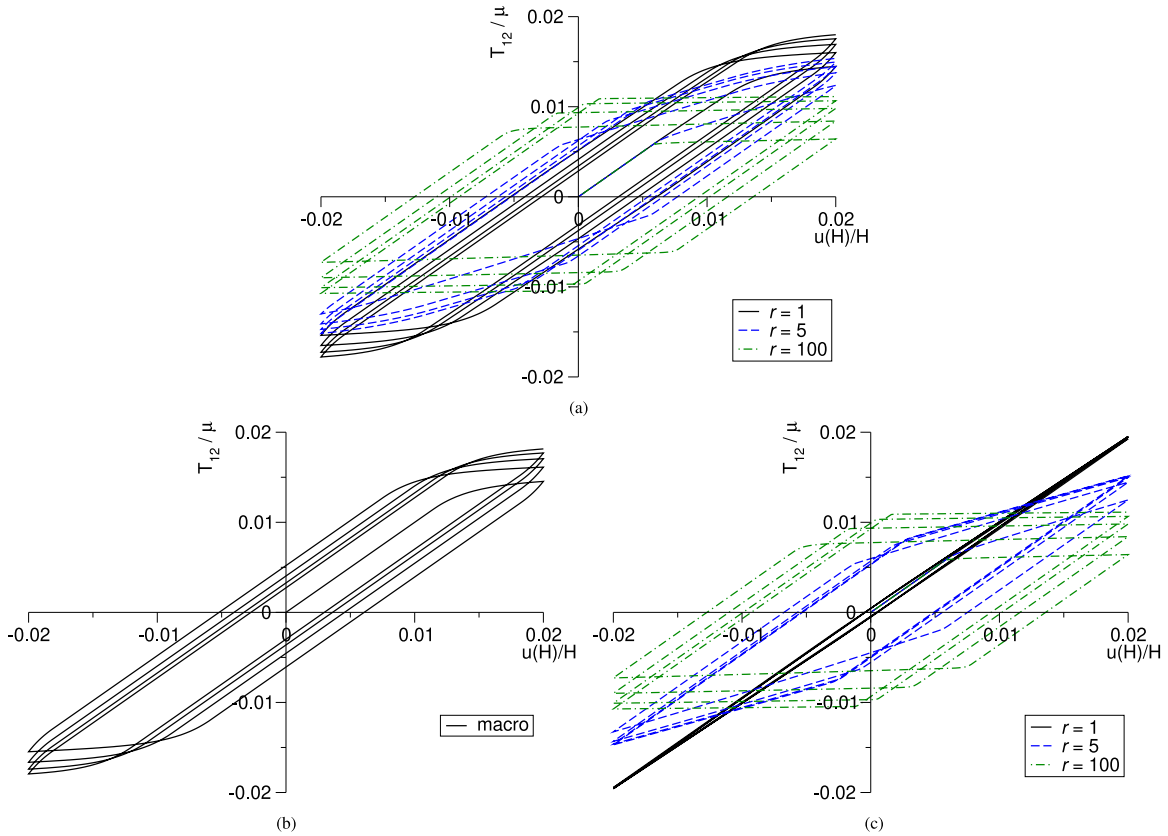

Fig. 4. Cyclic loading with hardening. Predictions of: (a) the m$\mathcal{M}$-model (M_4 in Table 2); (b) the $\mathcal{M}$-model (M_5 in Table 2); and (c) the m-model (M_6 in Table 2).

Table 3
Exponents b for a power-law regression of the curves in Fig. 8.

	Range of r	
	1−10	10−1000
	b	b
M_4	−0.32573	−0.035419
M_7	−0.082722	−0.030336
M_8	−0.26503	−0.035419
M_9	−0.29866	−0.024371

For small size, the data for the scaling parameter b obtained either through experiments (Mu et al., 2014; Zhang et al., 2023) or through pseudo-experimental DDD simulations (El-Awady et al., 2013; Cruzado et al., 2024; Amouzou-Adoun et al., 2024) may range between ≈−0.2 to ≈−0.9. The actual value of b depends, among several factors, on the initial density of dislocation sources, which enters the present phenomenological model only indirectly through parameters such as S_0 and κ_0. Higher-order SGP models from the literature that do not include very sophisticated, and computationally expensive, constitutive models and techniques usually predict too strong size dependence (e.g., $b \approx -1$). Scaling as strong as $b = -1$ is predicted by higher-order strain gradient *crystal* plasticity even in the presence of advanced nonlinear size-dependent kinematic hardening (Amouzou-Adoun et al., 2024). Although Table 3 already reports values of b interestingly of about −0.3, calibrating the value of the ratio κ_0/S_0 in the m$\mathcal{M}$-model may be sufficient to match experimental and DDD data on the scaling.

Next, Fig. 9 focuses on changing κ_0 while maintaining S_0 constant, that is, on the materials M_9, M_{10}, M_{11}, M_{12}, M_{13} in Table 4. As expected, the ratio $\kappa_0/S_0 > 1$ controls the scaling, which is reported in Table 5 and displays values of b ranging from ≈−0.1 to ≈−0.55. On the one hand, different values of the scaling exponent b can be obtained by calibrating κ_0/S_0 along with other material parameters. On the other hand, the obtained values already span a range that is significant in the light of experimental and DDD investigations. For instance, for a 45° inclined copper thin film inserted in a micropillar subjected to uniaxial compression, Mu

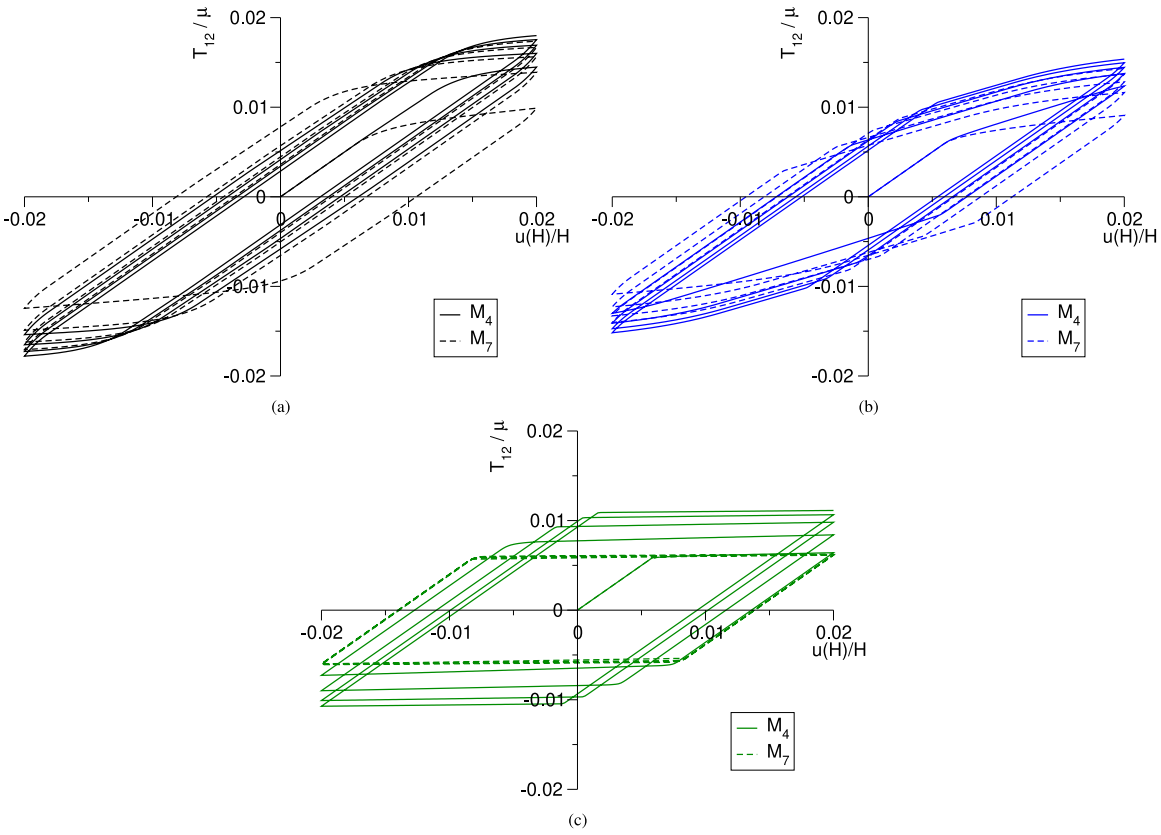

Fig. 5. Influence of κ_0 on cyclic loading for $\kappa_0 = 0.02\mu$ (M_4 in Table 2) and $\kappa_0 = 0.01\mu$ (M_7 in Table 2), with $S_0 = 0.01\mu$ and for three values of the normalized thickness r: (a) $r = 1$; (b) $r = 5$; and (c) $r = 100$.

et al. (2016) provide experimental values of b equal to −0.7 or −0.2, depending on whether the tested copper is annealed or not; for micropillars constituted by different additively manufactured alloys and subjected to uniaxial compression, Li et al. (2022) report b ranging from −0.12 to −0.24 depending on the alloy and the manufacturing technique (either laser powder bed fusion or directed energy deposition); for a planar polycrystal modeled with DDD, Balint et al. (2005) obtain a value of the scaling, referred to the Hall–Petch relation instead of Eq. (45), that changes from −0.4 to −0.45 by decreasing the initial dislocation source density of one order of magnitude; for the torsion of a FCC single crystal simulated with DDD, Cruzado et al. (2024) provide values of b ranging from −0.921 to 0.016 depending on the initial density of dislocation sources and the considered range of size; from the DDD simulations of Amouzou-Adoun et al. (2024) b is predicted to be equal to either −0.2 or −0.3 depending on the applied boundary conditions (either macroscopic shear or tension–compression). For completeness, Fig. 10 shows the locations of the apparent yield stress σ_Y on the stress–strain curves for the size $r = 1$ in Fig. 9.

From the foregoing analyses, it is concluded that the m$\mathcal{M}$-model has the capability to reproduce the size-dependence of the apparent yield stress observed in the literature.

4.3. Prediction of the results of discrete dislocation dynamics simulations

As a final analysis, some of the DDD results of Balint et al. (2005) are considered in detail. These DDD simulations are concerned with planar polycrystals constituted by square grains whose side has length equal to d. Each polycrystal is characterized by a different value of $d \in [0.2\ \mu\text{m}, 5\ \mu\text{m}]$ and is subjected to small-strain macroscopic pure shear, such as it is, in this investigation, an appropriate reference problem for examining the predictive capability of the phenomenological m$\mathcal{M}$ theory. In fact, the proposed simple-shear implementation of the m$\mathcal{M}$ theory can be used to model the *average* response of the grains in the polycrystals studied by Balint et al. (2005), where dislocations pile up at the grain boundaries and grains are subject to single slip randomly oriented along either of two orthogonal directions. Hence, the strip height H in the present FE model plays the role of the side d in the DDD simulations of Balint et al. (2005).

Specifically, here the focus is on the polycrystals denoted as low source density (LSD) polycrystals by Balint et al. (2005), which, with respect to the high source density (HSD) polycrystals, display stronger size-effect, encompassing not only strengthening but also increase of strain hardening with diminishing size. For the details on the material parameters adopted in the DDD simulations,

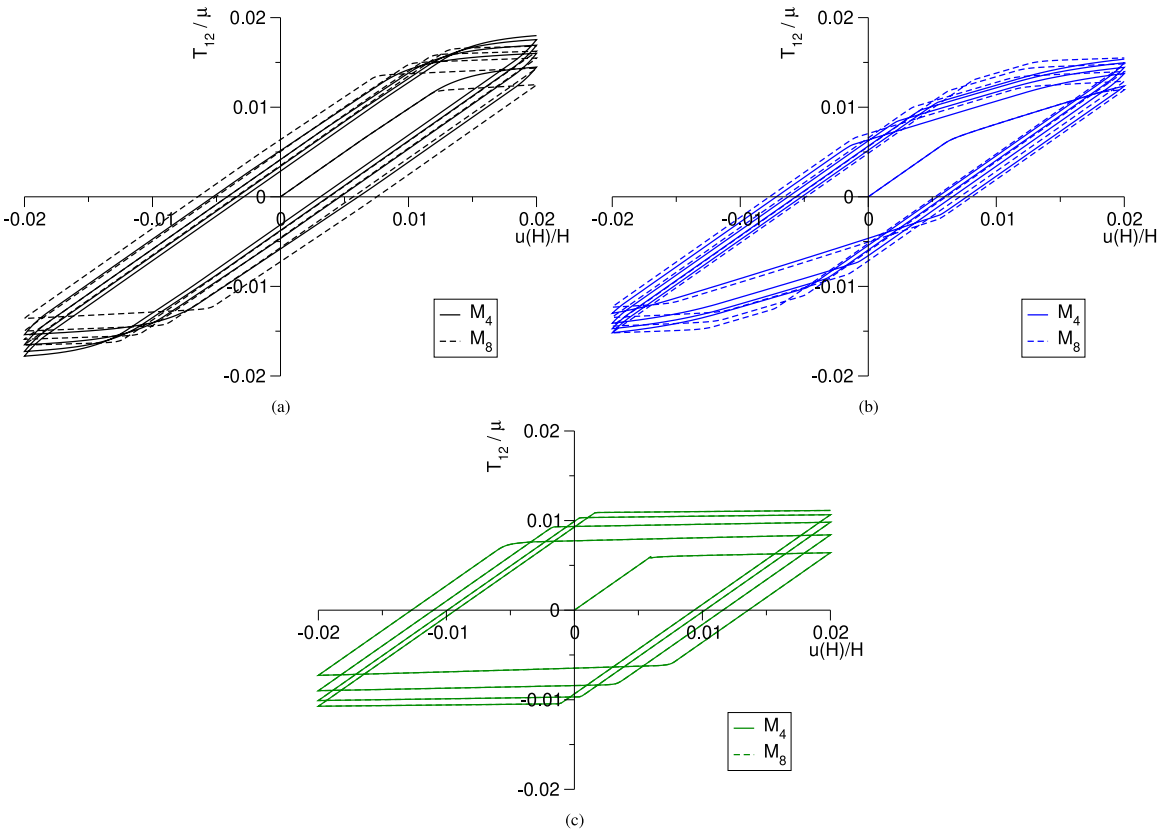

Fig. 6. Influence of b_1 on cyclic loading for $b_1 = 500$ (M_4 in Table 2) and $b_1 = 5000$ (M_8 in Table 2) for three values of the normalized thickness r: (a) $r = 1$; (b) $r = 5$; and (c) $r = 100$.

Table 4
List of parameters for different material sets M_i. The parameter that has been changed in M_{10}–M_{13} relative to the reference parameters in M_9 is highlighted in red.

Variable	M_9	M_{10}	M_{11}	M_{12}	M_{13}
b_1	500.	500.	500.	500.	500.
b_G	10.	10.	10.	10.	10.
κ_0	0.02μ	0.01μ	0.03μ	0.04μ	0.08μ
κ_s	0.04μ	0.04μ	0.04μ	0.04μ	0.08μ
m_κ	0.1	0.1	0.1	0.1	0.1
S_0	0.01μ	0.01μ	0.01μ	0.01μ	0.01μ
m_S	20.	20.	20.	20.	20.
$\Gamma_{\max}$	3.	3.	3.	3.	3.
a_G	5.	5.	5.	5.	5.

Table 5
Exponents b for a power-law regression of the curves in Fig. 9 (material sets $M_9, M_{10}, M_{11}, M_{12}, M_{13}$ in Table 4).

		Range of r	
		1–10	10–1000
	κ_0/S_0	b	b
M_{10}	1.	−0.093785	−0.020788
M_9	2.	−0.29866	−0.024371
M_{11}	3.	−0.41363	−0.028078
M_{12}	4.	−0.47392	−0.033432
M_{13}	8.	−0.54911	−0.11784

the reader is referred to Balint et al. (2005). Overall, Fig. 11a shows a very good agreement between the DDD results and the m$\mathcal{M}$-model predictions, with worst prediction for the largest sample.

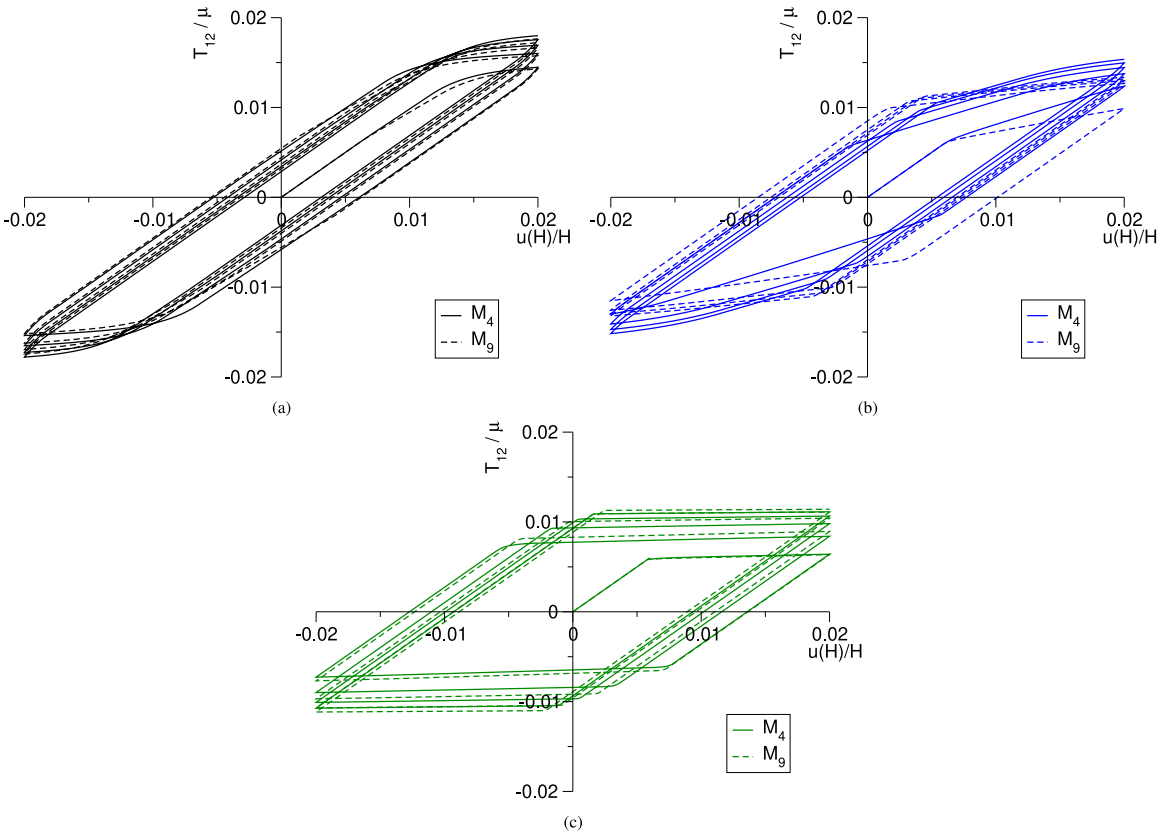

Fig. 7. Influence of $\Gamma_{\max}$ on cyclic loading for $\Gamma_{\max} = 1.5$ (M_4 in Table 2) and $\Gamma_{\max} = 3$. (M_9 in Table 2) for three values of the normalized thickness r: (a) $r = 1$; (b) $r = 5$; and (c) $r = 100$.

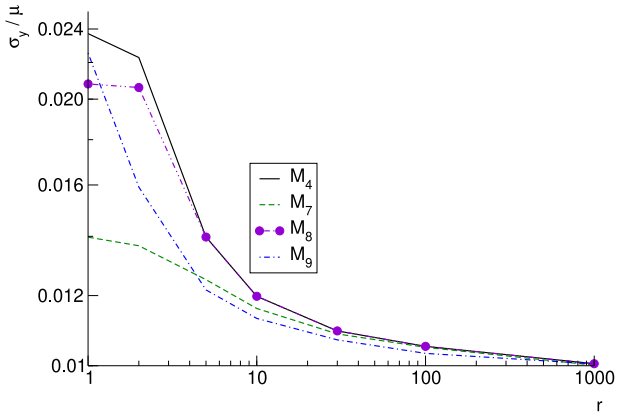

Fig. 8. Apparent yield stress scaling for different micro–macro materials in Table 2 (M_4, with $b_1 = 500.$, $\kappa_0 = 0.02\mu$, and $\Gamma_{\max} = 1.5$; M_7, with $\kappa_0 = 0.01\mu$; M_8, with $b_1 = 5000.$; M_9, with $\Gamma_{\max} = 3.$).

The results of Fig. 11 are obtained by using the material parameters recorded in Table 6, which are calibrated as follows. The shear modulus is computed directly from the Young modulus and Poisson's ratio provided by Balint et al. (2005). The calibration process has been simply conducted by following a trial-and-error approach, starting with a trial for the shear stress at initial yield, τ_y, of 25 MPa, as evaluated in Balint et al. (2005), to determine an initial estimate for $S_0 = \sqrt{3}\tau_y$. The value $\chi = 10$ has been kept fixed such as, on the basis of the results of the previous section and the data provided by Balint et al. (2005) for yield stress scaling, the trial values of κ_0 and κ_s were set to be three and four times S_0, respectively. A trial value for ℓ was identified by fitting the response of the three smallest strips. Then, the curves' fitting has been improved by increasing S_0 to correspond to an initial microscopic

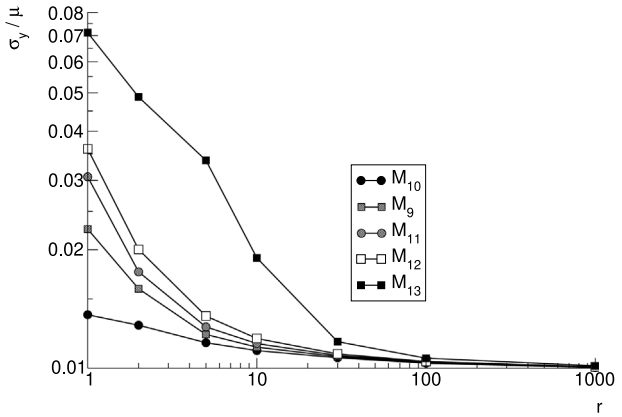

Fig. 9. Influence of κ_0 on the apparent yield stress scaling for $\kappa_0 = 0.01\mu$ (M_{10} in Table 4), $\kappa_0 = 0.02\mu$ (M_9 in Table 4), $\kappa_0 = 0.03\mu$ (M_{11} in Table 4), $\kappa_0 = 0.04\mu$ (M_{12} in Table 4), and $\kappa_0 = 0.08\mu$ (M_{13} in Table 4).

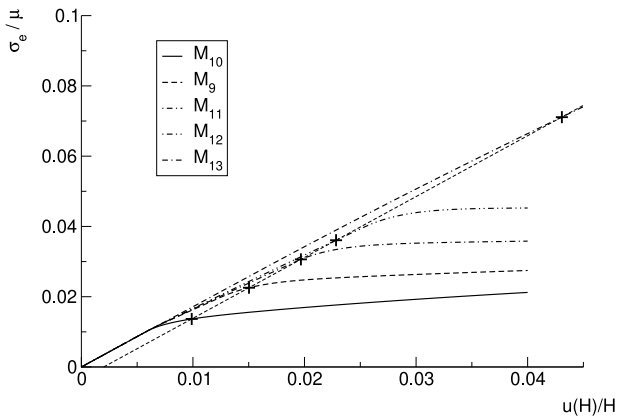

Fig. 10. Influence of κ_0 on the apparent yield stress for $\kappa_0 = 0.01\mu$ (M_{10} in Table 4), $\kappa_0 = 0.02\mu$ (M_9 in Table 4), $\kappa_0 = 0.03\mu$ (M_{11} in Table 4), $\kappa_0 = 0.04\mu$ (M_{12} in Table 4), and $\kappa_0 = 0.08\mu$ (M_{13} in Table 4): equivalent stress versus engineering shear strain curves under monotonic loading for $r = 1$; the apparent yield stress on each curve is identified with the plus symbol.

yield shear stress $\tau_y = 30$ MPa, along with suitable calibration of the hardening parameters m_s and m_κ. Although a more accurate calibration could be achieved both by using more advanced techniques, such as minimizing the error through a gradient-based procedure or employing evolutionary algorithms, and by optimizing over χ as well, this is beyond the scope of the present work. Here, the aim is to demonstrate that DDD results can be reasonably fitted by following a quite simple approach. Finally, it is worth mentioning that in the m$\mathcal{M}$ theory simulations macro-plasticity is activated only in the smallest sample ($H = 0.2\,\mu$m).

Fig. 11b shows the comparison in terms of yield stress scaling, which, again, is very satisfactory. It is important to notice that, by following Balint et al. (2005), here the definition of the apparent yield stress is different from the 0.2% offset rule adopted in the previous Section 4.2. In fact, in order to evaluate the yield stress scaling, Balint et al. (2005) compute the average of the shear stress (denoted as $\bar{\tau}$ in Balint et al., 2005, while here it is $\bar{T}_{12}$) over the effective engineering shear strain (denoted as γ in Balint et al., 2005, while here it is $u(H)/H$) ranging from 0.15% to 0.25%. Given that this average is needed to remove noise typical of DDD results that is absent in FE analyses, the $\bar{T}_{12}$ average of Balint et al. (2005) is compared in Fig. 11b with T_{12} evaluated at $u(H)/H = 0.2\%$ in the FE analyses. Moreover, Balint et al. (2005) evaluate the yield stress scaling by using the Hall–Petch relation, which, differently from Eq. (45), includes a reference yield stress referred to a sample large enough to be unaffected by the size-effect. By following this procedure, Balint et al. (2005) obtain a negative slope in the log–log plot equal to 0.4. Here, by fitting the power-law (45) on the data of Fig. 11b, the value of b is equal to -0.113 for the DDD results of Balint et al. (2005) and -0.109 for the results of present FE analyses, thus confirming the very satisfactory agreement.

5. Concluding remarks

This work investigates the m$\mathcal{M}$ theory developed in (Rubin and Bardella, 2023), which is used to model the size-dependent response of metals at the micro-scale. The m$\mathcal{M}$ theory is developed in an Eulerian finite-deformation framework and extends the

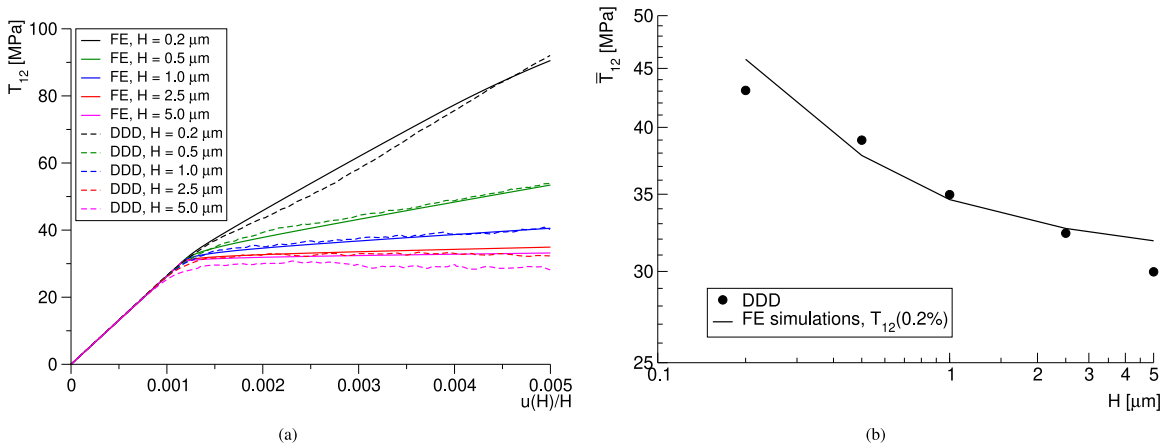

Fig. 11. Predictions of the DDD results of Balint et al. (2005) on LSD polycrystals: (a) stress–strain curves and (b) yield stress scaling. Note that in Balint et al. (2005) H is the grain size and is denoted as d.

Table 6
Material parameters used to predict the DDD results of Balint et al. (2005), as shown in Fig. 11. Note that the value of the parameter χ is equal to 10, as always in this investigation (as well as $k_2 = k_3 = 10$).

μ	26.316 GPa
ℓ	0.12 μm
b_1	500.
b_G	10.
κ_0	129.9 MPa
κ_s	173.2 MPa
m_κ	0.1
S_0	51.96 MPa
m_S	8.
$\Gamma_{\max}$	3.
a_G	5.

elastoplasticity in (Rubin and Attia, 1996) by using two distinct plastic rate tensors, contributing to the so-called micro- and macro-plasticity fields. Each of these fields develops on the basis of a specific rate-independent smooth transition between the elastic and plastic regimes. Macro-plasticity is standard and its smooth transition follows Hollenstein et al. (2013, 2015). Micro-plasticity is governed by a higher-order balance equation modifying that characterizing the strain gradient plasticity (SGP) of Gurtin (2004), thus being size-dependent on the basis of the evolution of a Nye–Kröner-like dislocation density tensor (Nye, 1953; Kröner, 1962).

One of the main ideas of the m$\mathcal{M}$ theory relies on the experimental observation of Maaß and Derlet (2018), where "micro-plasticity" consists of tiny irreversible deformations occurring before the stress reaches the *apparent* yield stress. Similarly, in the m$\mathcal{M}$ theory the micro-yield stress is deliberately set lower than the macro-yield stress, allowing micro-plasticity to control the increase of the *apparent* yield stress with diminishing specimen size.

This investigation focuses on the yield stress scaling and the response under multiple cycles predicted by the m$\mathcal{M}$ theory. To this purpose, a user element subroutine (`uel`) for small strains and rotations in constrained simple shear has been developed and implemented in ABAQUS/Simulia (Dassault Systèmes, 2013) to study the response of the m$\mathcal{M}$ theory including micro- and macro-plasticity hardening (neglected in the results of Rubin and Bardella, 2023, additionally obtained for monotonic loading only). To remove an unphysical response observed in cyclic loading using the original formulation (Rubin and Bardella, 2023), the function Γ_G controlling the smooth transition between the elastic and micro-plastic regimes has been modified. Specifically, here Γ_G is proposed to be a monotonically increasing function of the loading history, up to a saturated value.

The size-dependent response is studied for strain-controlled cycles. The results demonstrate flexibility of the m$\mathcal{M}$ theory to model material responses that are relevant to polycrystal metal plasticity at sizes where geometrically necessary dislocations (Ashby, 1970) play a role. This is due to the non-trivial interplay between micro- and macro-plasticity.

As a key contribution of this work, it is shown that the m$\mathcal{M}$ theory can describe the *apparent* yield stress scaling observed in small-scale metal plasticity through experiments (e.g., Dunstan and Bushby, 2014; Mu et al., 2016) and discrete dislocation dynamics (DDD) simulations (e.g., Biner and Morris, 2002; Balint et al., 2005; El-Awady et al., 2013; Cruzado et al., 2024; Amouzou-Adoun et al., 2024). This control is achieved even though the proposed theory only considers the simplest treatment of the gradient of the plastic flow, with an associated quadratic defect energy. On the one hand, this simplicity is advantageous, as it makes the

size-dependent theory relatively easy to work with, in contrast to the more complex higher-order constitutive models developed in the literature since the work of Dahlberg and Ortiz (2019) and Panteghini et al. (2019) to predict experimental size-effects without encountering thermodynamic inconsistencies or anomalous behaviors (as discussed by Gudmundson, 2004, and Fleck et al., 2014). On the other hand, this contribution paves the way to the development of new models with enhanced capabilities, that could be obtained by adopting a more sophisticated treatment of micro-plastic strain gradients (Panteghini et al., 2019).

To further demonstrate the capability of the m$\mathcal{M}$ theory to model the size-dependent response of metals, the m$\mathcal{M}$ theory is successfully employed to predict the stress–strain curves obtained by Balint et al. (2005) through DDD simulations of the response under macroscopic pure shear of planar polycrystals with variable grains' size.

The major open issue for the m$\mathcal{M}$ theory is the study of its response for finite deformations. In particular, the outcome of the proposed evolution Eq. (4) for the Nye–Kröner-like dislocation density tensor needs to be explored. Additionally, the application to boundary value problems more complex than the constrained simple shear is planned for future studies.

CRediT authorship contribution statement

Andrea Panteghini: Writing – review & editing, Writing – original draft, Visualization, Validation, Software, Methodology, Investigation, Data curation, Conceptualization. **Lorenzo Bardella:** Writing – review & editing, Writing – original draft, Validation, Supervision, Methodology, Investigation, Formal analysis, Conceptualization. **M.B. Rubin:** Writing – review & editing, Writing – original draft, Supervision, Investigation, Conceptualization.

Declaration of competing interest

The authors declare that they have no known competing financial interests or personal relationships that could have appeared to influence the work reported in this paper.

Acknowledgments

The finite element code ABAQUS/Simulia has been run at the Department of Civil, Environmental, Architectural Engineering and Mathematics, University of Brescia, Italy, under an academic license. A.P. and L.B. acknowledge the support of the Italian Ministry of Education, University, and Research (MIUR). Work done under the auspices of GNFM (Gruppo Nazionale per la Fisica Matematica) of INDAM (Istituto Nazionale di Alta Matematica Francesco Severi). All authors approved the version of the manuscript to be published.

Appendix A. Consistent FE stiffness matrix

The stiffness matrix $\mathbf{K}$, which is employed to solve the nonlinear algebraic system obtained by equating the internal forces (43) to the external forces, is defined as the differentiation of the vectors of the internal nodal forces in Eq. (43) with respect to the incremental nodal variables, and it is given by

$$\mathbf{K}=\begin{bmatrix}\mathbf{K}_{u,u} & \mathbf{K}_{u,g_{12}} & \mathbf{K}_{u,g_{21}}\\ \mathbf{K}_{g_{12},u} & \mathbf{K}_{g_{12},g_{12}} & \mathbf{K}_{g_{12},g_{21}}\\ \mathbf{K}_{g_{21},u} & \mathbf{K}_{g_{21},g_{12}} & \mathbf{K}_{g_{21},g_{21}}\end{bmatrix}$$

where, by using ${}_S g_{12}=(g_{12}+g_{21})/2$ and ${}_{SK} g_{12}=(g_{12}-g_{21})/2$,

$$\mathbf{K}_{u,u}=\int_0^H \frac{1}{2}\frac{\partial T_{12}}{\partial \epsilon_{12}}\mathbf{B}^T\mathbf{B}\,\mathrm{d}x_2\,,\quad \mathbf{K}_{u,g_{12}}=\mathbf{K}_{u,g_{21}}=\int_0^H \frac{1}{2}\frac{\partial T_{12}}{\partial {}_S g_{12}}\mathbf{B}^T\mathbf{N}\,\mathrm{d}x_2$$

$$\mathbf{K}_{g_{12},u}=\int_0^H \frac{1}{2}\left(\frac{\partial {}_S S_{12}}{\partial \epsilon_{12}}+\frac{\partial {}_{SK} S_{12}}{\partial \epsilon_{12}}-\frac{\partial \Gamma_G}{\partial \epsilon_{12}}T_{12}-\frac{\partial T_{12}}{\partial \epsilon_{12}}\Gamma_G\right)\mathbf{N}^T\mathbf{B}\,\mathrm{d}x_2$$

$$\mathbf{K}_{g_{12},g_{12}}=\int_0^H \frac{1}{2}\left(\frac{\partial {}_S S_{12}}{\partial {}_S g_{12}}+\frac{\partial {}_{SK} S_{12}}{\partial {}_S g_{12}}+\frac{\partial {}_S S_{12}}{\partial {}_{SK} g_{12}}+\frac{\partial {}_{SK} S_{12}}{\partial {}_{SK} g_{12}}-\frac{\partial \Gamma_G}{\partial {}_S g_{12}}T_{12}-\frac{\partial T_{12}}{\partial {}_S g_{12}}\Gamma_G\right)\mathbf{N}^T\mathbf{N}\,\mathrm{d}x_2$$

$$\mathbf{K}_{g_{12},g_{21}}=\int_0^H \frac{1}{2}\left(\frac{\partial {}_S S_{12}}{\partial {}_S g_{12}}+\frac{\partial {}_{SK} S_{12}}{\partial {}_S g_{12}}-\frac{\partial {}_S S_{12}}{\partial {}_{SK} g_{12}}-\frac{\partial {}_{SK} S_{12}}{\partial {}_{SK} g_{12}}-\frac{\partial \Gamma_G}{\partial {}_S g_{12}}T_{12}-\frac{\partial T_{12}}{\partial {}_S g_{12}}\Gamma_G\right)\mathbf{N}^T\mathbf{N}\,\mathrm{d}x_2$$

$$\mathbf{K}_{g_{21},u}=\int_0^H \frac{1}{2}\left(\frac{\partial {}_S S_{12}}{\partial \epsilon_{12}}-\frac{\partial {}_{SK} S_{12}}{\partial \epsilon_{12}}-\frac{\partial \Gamma_G}{\partial \epsilon_{12}}T_{12}-\frac{\partial T_{12}}{\partial \epsilon_{12}}\Gamma_G\right)\mathbf{N}^T\mathbf{B}\,\mathrm{d}x_2$$

$$\mathbf{K}_{g_{21},g_{12}}=\int_0^H \frac{1}{2}\left(\frac{\partial {}_S S_{12}}{\partial {}_S g_{12}}-\frac{\partial {}_{SK} S_{12}}{\partial {}_S g_{12}}+\frac{\partial {}_S S_{12}}{\partial {}_{SK} g_{12}}-\frac{\partial {}_{SK} S_{12}}{\partial {}_{SK} g_{12}}-\frac{\partial \Gamma_G}{\partial {}_S g_{12}}T_{12}-\frac{\partial T_{12}}{\partial {}_S g_{12}}\Gamma_G\right)\mathbf{N}^T\mathbf{N}\,\mathrm{d}x_2$$

$$\mathbf{K}_{g_{21},g_{21}}=\int_0^H \left[\frac{1}{2}\left(\frac{\partial {}_S S_{12}}{\partial {}_S g_{12}}-\frac{\partial {}_{SK} S_{12}}{\partial {}_S g_{12}}-\frac{\partial {}_S S_{12}}{\partial {}_{SK} g_{12}}+\frac{\partial {}_{SK} S_{12}}{\partial {}_{SK} g_{12}}-\frac{\partial \Gamma_G}{\partial {}_S g_{12}}T_{12}-\frac{\partial T_{12}}{\partial {}_S g_{12}}\Gamma_G\right)\mathbf{N}^T\mathbf{N}+\tilde{\mu}\ell^2\mathbf{C}^T\mathbf{C}\right]\,\mathrm{d}x_2$$

It is finally observed that the computation of the foregoing derivatives of the stresses ${}_S S_{12}$, ${}_{SK} S_{12}$, T_{12}, and of Γ_G is standard. These derivatives are obtained through the implicit differentiation of the constitutive Newton's residuals provided in Eqs. (32) and (33) of Section 3.

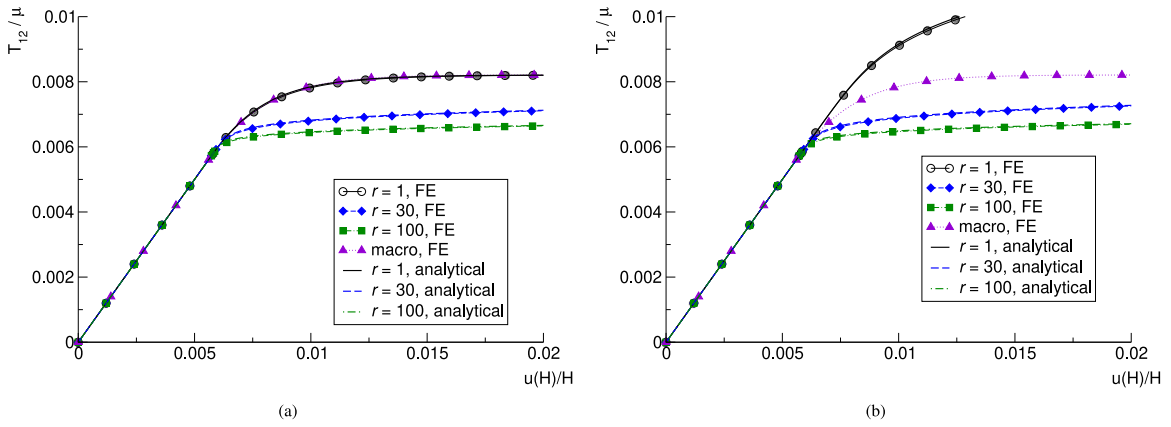

Fig. B.1. Monotonic loading. Comparison of the responses predicted by the semi-analytical results in (Rubin and Bardella, 2023) and the FE predictions for three ratios $r = H/\ell$ without hardening: (a) the m$\mathcal{M}$-model (V_1 in Table 1); and (b) m-model (V_3 in Table 1). The $\mathcal{M}$-model (V_2 in Table 1) is included for comparison although it is not a bound for the m-model in (b).

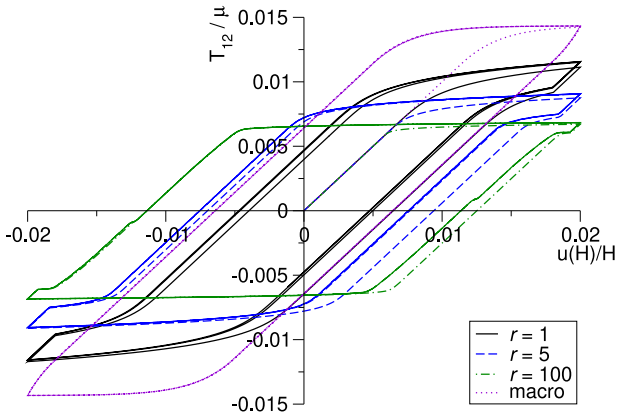

Fig. C.1. Cyclic loading without hardening showing unphysical response predicted by the m$\mathcal{M}$-model using the function Γ_G^{R} in Eq. (21) (M_1^{R} in Table 2). The $\mathcal{M}$-model (M_2 in Table 2) is included for comparison.

Appendix B. Validation of the finite element implementation

Fig. B.1 compares the semi-analytical results in (Rubin and Bardella, 2023), that are obtained in the absence of hardening ($m_\kappa = m_S = 0$), with the FE predictions for three ratios $r = H/\ell$. Fig. B.1a shows the predictions of the responses for the m$\mathcal{M}$-model (V_1 in Table 1) and Fig. B.1b focuses on the responses for the m-model (V_3 in Table 1). Predictions of the $\mathcal{M}$-model (V_2 in Table 1) are included for comparison. As recorded in the last row of Table 1, these responses are all derived by using $\Gamma_G = \Gamma_G^{\mathrm{R}}$ in Eq. (21). The near perfect overlap in the semi-analytical and FE results verifies the accuracy and reliability of the FE implementation.

Appendix C. On the need to modify the micro-plastic smooth transition with respect to that in (Rubin and Bardella, 2023)

In a first attempt to model strain-controlled cyclic loading without hardening use was made of the functional form of Γ_G given by Γ_G^{R} in (21) proposed in (Rubin and Bardella, 2023). This form allows for a smooth elastic–inelastic transition for micro-plasticity during monotonic loading. However, from Fig. C.1, which displays responses obtained with the set of parameters M_1^{R} in Table 2, it can be seen that $\Gamma_G = \Gamma_G^{\mathrm{R}}$ produces unphysical behavior during unloading because Γ_G^{R} goes suddenly to zero as σ_e reduces. From inspection of the higher-order balance equations (27) and (28), it can be deduced that this requires an anomalous behavior of the micro-plastic field. Also, when Γ_G^{R} becomes zero upon loading reversal, any value of $\mathbf{G} \equiv \dot{\mathbf{g}}$ maintains vanishing micro-plasticity rate $\Gamma_G^{\mathrm{R}}\mathbf{G}$, thus leading to numerical complications since the components of $\mathbf{G}$ are used to establish the FE DOFs. Fig. C.1 includes the prediction of the $\mathcal{M}$-model (M_2 in Table 2) for comparison. On the basis of these results, the modified form of Γ_G in Eq. (22) is proposed to ensure that Γ_G is a monotonically increasing function. This modification guarantees that once micro-plasticity is activated it remains active if $\dot{\mathbf{g}} \neq \mathbf{0}$ from the solution of Eqs. (27) and (28).

Data availability

Data will be made available on request.

References

Amouzou-Adoun, Y.A., Jebahi, M., Forest, S., Fivel, M., 2024. Advanced modeling of higher-order kinematic hardening in strain gradient crystal plasticity based on discrete dislocation dynamics. J. Mech. Phys. Solids 193, 105875.

Anand, L., Gurtin, M.E., Lele, S.P., Gething, C., 2005. A one-dimensional theory of strain-gradient plasticity: formulation, analysis, numerical results. J. Mech. Phys. Solids 53, 1789–1826.

Arora, A., Arora, R., Acharya, A., 2022. Mechanics of micropillar confined thin film plasticity. Acta Mater. 238, 118192.

Arsenlis, A., Parks, D.M., 1999. Crystallographic aspects of geometrically-necessary and statistically-stored dislocation density. Acta Mater. 47 (5), 1597–1611.

Ashby, M.F., 1970. The deformation of plastically non-homogeneous materials. Phil. Mag. 21, 399–424.

Balint, D.S., Deshpande, V.S., Needleman, A., Van der Giessen, E., 2005. A discrete dislocation plasticity analysis of grain-size strengthening. Mater. Sci. Eng. A 400–401, 186–190.

Bardella, L., 2009. A comparison between crystal and isotropic strain gradient plasticity theories with accent on the role of the plastic spin. Eur. J. Mech. A Solids 28 (3), 638–646.

Bardella, L., 2010. Size effects in phenomenological strain gradient plasticity constitutively involving the plastic spin. Internat. J. Engrg. Sci. 48 (5), 550–568.

Bardella, L., 2021. On a mixed energetic–dissipative constitutive law for non-proportional loading, with focus on small-scale plasticity. Proc. R. Soc. A 477 (2248), 20200940.

Bardella, L., Panteghini, A., 2015. Modelling the torsion of thin metal wires by distortion gradient plasticity. J. Mech. Phys. Solids 78, 467–492.

Bertram, A., 2023. Compendium on Gradient Materials. Springer, Cham.

Bilby, B.A., Gardner, L.R.T., Stroh, A.N., 1957. Continuous distributions of dislocations and the theory of plasticity. In: Proceedings of the 9th International Congress of Applied Mechanics. vol. 9, University de Brussels, pp. 35–44.

Biner, S.B., Morris, J.R., 2002. A two-dimensional discrete dislocation simulation of the effect of grain size on strengthening behaviour. Modelling Simul. Mater. Sci. Eng. 10 (6), 617.

Bittencourt, E., Needleman, A., Gurtin, M.E., van der Giessen, E., 2003. A comparison of nonlocal continuum and discrete dislocation plasticity predictions. J. Mech. Phys. Solids 51, 281–310.

Chiricotto, M., Giacomelli, L., Tomassetti, G., 2016. Dissipative scale effects in strain-gradient plasticity: the case of simple shear. SIAM J. Appl. Math. 76 (2), 688–704.

Cosserat, E., Cosserat, F., 1909. Théorie des Corps Déformables. Hermann, Paris.

Cruzado, A., Ariza, M.P., Needleman, A., Ortiz, M., Benzerga, A.A., 2024. A discrete dislocation analysis of size-dependent plasticity in torsion. J. Mech. Phys. Solids 190, 105709.

Dahlberg, C., Ortiz, M., 2019. Fractional strain-gradient plasticity. Eur. J. Mech. A Solids 75, 348–354.

Dassault Systèmes, 2013. ABAQUS User's & Theory Manuals — Release 6.13-1. Providence, RI, USA.

Dunstan, D.J., Bushby, A.J., 2014. Grain size dependence of the strength of metals: The Hall–Petch effect does not scale as the inverse square root of grain size. Int. J. Plast. 53, 56–65.

Ebobisse, F., Hackl, K., Neff, P., 2019. A canonical rate-independent model of geometrically linear isotropic gradient plasticity with isotropic hardening and plastic spin accounting for the Burgers vector. Contin. Mech. Therm. 31, 1477–1502.

El-Awady, J.A., Uchic, M.D., Shade, P.A., Kim, S.-L., Rao, S.I., Dimiduk, D.M., Woodward, C., 2013. Pre-straining effects on the power-law scaling of size-dependent strengthening in ni single crystals. Scr. Mater. 68 (3), 207–210.

El-Naaman, S., Nielsen, K., Niordson, C., 2019. An investigation of back stress formulations under cyclic loading. Mech. Mater. 130, 76–87.

Eringen, A.C., 1999. Microcontinuum Field Theories: I. Foundations and Solids. Springer, New York.

Fleck, N.A., Hutchinson, J.W., 1997. Strain gradient plasticity. Adv. Appl. Mech. 33, 295–361.

Fleck, N.A., Hutchinson, J.W., Willis, J.R., 2014. Strain gradient plasticity under non-proportional loading. Proc. R. Soc. A 470, 20140267.

Fleck, N.A., Muller, G.M., Ashby, M.F., Hutchinson, J.W., 1994. Strain gradient plasticity: theory and experiments. Acta Metall. Mater. 42, 475–487.

Forest, S., 2008. Some links between Cosserat, strain gradient crystal plasticity and the statistical theory of dislocations. Phil. Mag. 88 (30–32), 3549–3563.

Forest, S., 2020. Continuum thermomechanics of nonlinear micromorphic, strain and stress gradient media. Philos. Trans. R. Soc. Lond. Ser. A Math. Phys. Eng. Sci. 378, 20190169.

Forest, S., Guéninchault, N., 2013. Inspection of free energy functions in gradient crystal plasticity. Acta Mech. Sin. 29 (6), 763–772.

Forest, S., Sievert, R., 2003. Elastoviscoplastic constitutive frameworks for generalized continua. Acta Mech. 160, 71–111.

Green, A.E., Naghdi, P.M., 1995. A unified procedure for construction of theories of deformable media. II. Generalized continua. Proc. R. Soc. Lond. Ser. A Math. Phys. Eng. Sci. 448, 357–377.

Greer, J.R., De Hosson, J.T., 2011. Plasticity in small-sized metallic systems: Intrinsic versus extrinsic size effect. Prog. Mater. Sci. 56 (6), 654–724.

Gudmundson, P., 2004. A unified treatment of strain gradient plasticity. J. Mech. Phys. Solids 52, 1379–1406.

Gurtin, M.E., 2004. A gradient theory of small-deformation isotropic plasticity that accounts for the Burgers vector and for dissipation due to plastic spin. J. Mech. Phys. Solids 52 (11), 2545–2568.

Gurtin, M.E., Anand, L., 2005. A gradient theory of strain-gradient plasticity for isotropic, plastically irrotational materials. Part I: Small deformations. J. Mech. Phys. Solids 53, 1624–1649.

Hall, E.O., 1951. The deformation and ageing of mild steel: III discussion of results. Proc. Phys. Soc. B 64, 747–753.

Hirschberger, C.B., Steinmann, P., 2009. Classification of concepts in thermodynamically consistent generalized plasticity. J. Eng. Mech. 135 (3), 156–170.

Hollenstein, M., Jabareen, M., Rubin, M.B., 2013. Modeling a smooth elastic–inelastic transition with a strongly objective numerical integrator needing no iteration. Comput. Mech. 52, 649–667.

Hollenstein, M., Jabareen, M., Rubin, M.B., 2015. Erratum to: Modeling a smooth elastic–inelastic transition with a strongly objective numerical integrator needing no iteration. Comput. Mech. 55, 453–453.

Khandagale, P., Liu, L., Sharma, P., 2024. Statistical mechanics of plasticity: Elucidating anomalous size-effects and emergent fractional nonlocal continuum behavior. J. Mech. Phys. Solids 191, 105747.

Kröner, E., 1959. General continuum theory of dislocations and intrinsic stresses. Arch. Ration. Mech. Anal. 4, 273–334.

Kröner, E., 1962. Dislocations and continuum mechanics. Appl. Mech. Rev. 15, 599–606.

Kuroda, M., Needleman, A., 2023. Non-quadratic strain gradient plasticity theory and size effects in constrained shear. Trans. ASME, J. Appl. Mech. 90 (12), 121004.

Kuroda, M., Tvergaard, V., Needleman, A., 2021. Constraint and size effects in confined layer plasticity. J. Mech. Phys. Solids 149, 104328.

Lee, E.H., 1969. Elastic–plastic deformation at finite strains. Trans. ASME, J. Appl. Mech. 36, 1–6.

Li, S.-H., Zhao, Y., Radhakrishnan, J., Ramamurty, U., 2022. A micropillar compression investigation into the plastic flow properties of additively manufactured alloys. Acta Mater. 240, 118290.
Liu, D., He, Y., Dunstan, D.J., Zhang, B., Gan, Z., Hu, P., Ding, H., 2013. Anomalous plasticity in cyclic torsion of micron scale metallic wires. Phys. Rev. Lett. 110, 244301.
Maaß, R., Derlet, P., 2018. Micro-plasticity and recent insights from intermittent and small-scale plasticity. Acta Mater. 143, 338–363.
Maugin, G., 1979. Nonlocal-theories or gradient-type theories: A matter of convenience. Arch. Mech. 31 (1), 15–26.
Mindlin, R.D., 1964. Microstructure in linear elasticity. Arch. Ration. Mech. Anal. 16, 51–78.
Mu, Y., Hutchinson, J., Meng, W., 2014. Micro-pillar measurements of plasticity in confined cu thin films. Extreme Mech. Lett. 1, 62–69.
Mu, Y., Zhang, X., Hutchinson, J., Meng, W., 2016. Dependence of confined plastic flow of polycrystalline cu thin films on microstructure. MRS Commun. 6 (3), 289–294.
Nédélec, J.C., 1980. Mixed finite elements in $\Re^3$. Numer. Math. 35 (3), 315–341.
Nielsen, K.L., Niordson, C.F., 2014. A numerical basis for strain-gradient plasticity theory: Rate-independent and rate-dependent formulations. J. Mech. Phys. Solids 63, 113–127.
Nielsen, K.L., Niordson, C.F., 2019. A finite strain FE-implementation of the fleck-willis gradient theory: Rate-independent versus visco-plastic formulation. Eur. J. Mech. A Solids 75, 389–398.
Niordson, C.F., Hutchinson, J.W., 2003. On lower order strain gradient plasticity theories. Eur. J. Mech. A Solids 22 (6), 771–778.
Nye, J.F., 1953. Some geometrical relations in dislocated crystals. Acta Metall. 1, 153–162.
Ohno, N., Okumura, D., 2007. Higher-order stress and grain size effects due to self-energy of geometrically necessary dislocations. J. Mech. Phys. Solids 55, 1879–1898.
Panteghini, A., Bardella, L., 2016. On the finite element implementation of higher-order gradient plasticity, with focus on theories based on plastic distortion incompatibility. Comput. Methods Appl. Math. 310, 840–865.
Panteghini, A., Bardella, L., 2018. On the role of higher-order conditions in distortion gradient plasticity. J. Mech. Phys. Solids 118, 293–321.
Panteghini, A., Bardella, L., 2020. Modelling the cyclic torsion of polycrystalline micron-sized copper wires by distortion gradient plasticity. Phil. Mag. 100 (18), 2352–2364.
Panteghini, A., Bardella, L., Niordson, C.F., 2019. A potential for higher-order phenomenological strain gradient plasticity to predict reliable response under non-proportional loading. Proc. R. Soc. A 475 (2229), 20190258.
Petch, N.J., 1953. The cleavage strength of polycrystals. J. Iron Steel Inst. 174, 25–28.
Poh, L.H., Peerlings, R.H.J., 2016. The plastic rotation effect in an isotropic gradient plasticity model for applications at the meso scale. Int. J. Solids Struct. 78–79, 57–69.
Rognes, M.E., Kirby, R.C., Logg, A., 2010. Efficient assembly of $H(\mathrm{div})$ and $H(\mathrm{curl})$ conforming finite elements. SIAM J. Sci. Comput. 31 (6), 4130–4151.
Rubin, M.B., 1996. On the treatment of elastic deformation in finite elastic-viscoplastic theory. Int. J. Plast. 12, 951–965.
Rubin, M.B., 2012. Removal of unphysical arbitrariness in constitutive equations for elastically anisotropic nonlinear elastic–viscoplastic solids. Internat. J. Engrg. Sci. 53, 38–45.
Rubin, M.B., 2021. Continuum Mechanics with Eulerian Formulations of Constitutive Equations. Springer Nature.
Rubin, M.B., Attia, A.V., 1996. Calculation of hyperelastic response of finitely deformed elastic-viscoplastic materials. Int. J. Numer. Methods Biomed. Eng. 39, 309–320.
Rubin, M., Bardella, L., 2023. An Eulerian thermodynamical formulation of size-dependent plasticity. J. Mech. Phys. Solids 170, 105122.
Rubin, M., Bardella, L., 2024. Eulerian rates of elastic incompatibilities applied to size-dependent hardening in finite torsion. J. Mech. Phys. Solids 193, 105905.
Svendsen, B., Bargmann, S., 2010. On the continuum thermodynamic rate variational formulation of models for extended crystal plasticity at large deformation. J. Mech. Phys. Solids 58, 1253–1271.
Wieners, C., Wohlmuth, B., 2011. A primal–dual finite element approximation for a nonlocal model in plasticity. SIAM J. Numer. Anal. 49, 692–710.
Willis, J.R., 2019. Some forms and properties of models of strain-gradient plasticity. J. Mech. Phys. Solids 123, 348–356.
Zhang, B., Nielsen, K., Hutchinson, J., Meng, W., 2023. Toward the development of plasticity theories for application to small-scale metal structures. Proc. Natl. Acad. Sci. USA 201 (44), e2312538120.